THESIS FOR THE DEGREE OF DOCTOR OF PHILOSOPHY

Fatigue crack behaviour in pearlitic railway rails subjected to large shear deformation

DANIEL GREN

Department of Industrial and Materials Science
Division of Engineering Materials
CHALMERS UNIVERSITY OF TECHNOLOGY
Gothenburg, Sweden 2024

Fatigue crack behaviour in pearlitic railway rails subjected to large shear deformation
DANIEL GREN
ISBN 978-91-8103-069-3

Doktorsavhandlingar vid Chalmers tekniska högskola
Ny serie nr. 5527
ISSN 0346-718X
Department of Industrial and Materials Science
Division of Engineering Materials
Chalmers University of Technology
SE-412 96 Gothenburg
Sweden
Telephone: +46 (0)31-772 1000

Cover:
Crack path and strain field of predeformed material subjected to multiaxial loading.

Printed by Chalmers Digitaltryck
Gothenburg, Sweden 2024

Fatigue crack behaviour in pearlitic railway rails subjected to large shear deformation
Thesis for the degree of Doctor of Philosophy
DANIEL GREN
Department of Industrial and Materials Science
Division of Engineering Materials
Chalmers University of Technology

Abstract

The impacts from global warming and climate change continue to rise, and securing the needs of future generations requires a transition to a climate-neutral society. Rail transportation, as one of the safest and most energy-efficient modes of transportation, offers a sustainable alternative to fossil-fuel-based transportation. There are, however, many challenges that must be addressed for rail transportation to be a more competitive option. Safety, functionality, reliability, and economic feasibility must be ensured. The major challenge related to materials is rolling contact fatigue, which impairs safety and economic reliability. The imposed loadings from the wheel/rail contact induce severe deformations in the near-surface region of the rail, leading to the formation of an aligned and anisotropic microstructure. Rolling contact fatigue cracks are often initiated in this region, and crack propagation is affected by the direction of the microstructure alignment.

The aim of this thesis work is to better understand how the anisotropy developing in service changes the fatigue and fracture characteristics of rail steels. Fatigue crack propagation experiments under uniaxial, pulsating torsional, and non-proportional multiaxial loading, on both virgin and predeformed pearlitic rail steel R260 have been conducted. The material state of the predeformed material is similar to the material state in the near surface of used rails and was obtained by bi-axial large shear deformation under compression.

The uniaxial and torsional fatigue crack propagation experiments showed that the fatigue life is dependent on the material state, with predeformed material exhibiting a longer fatigue life. The effect of predeformation on the crack growth direction was limited in uniaxial loading but dependent on the material state in torsional loading. For the multiaxial fatigue crack propagation experiments, the crack growth direction was significantly influenced by predeformation. The early crack growth rate was found to be similar for both the undeformed and predeformed material states. In addition to these experiments, in-situ fatigue crack propagation experiments were also conducted on single edge notched specimens machined from predeformed test bars along two different directions. This was a first attempt to characterize the effect of microstructure alignment locally on the crack growth and crack paths. Lastly, a method for in-field railhead crack detection using digital image correlation was proposed. The method was evaluated under laboratory conditions, and the detected cracks correlated well with the crack network in the analyzed rail section.

Keywords: Pearlitic steel, Fatigue crack propagation, Torsional loading, Uniaxial loading, Multiaxial loading, Predeformation, Anisotropy

Till min kära Erica, min familj och mina vänner

Preface

This doctoral thesis was carried out at the Department of Industrial and Materials Science at Chalmers University of Technology from June 2019 to May 2024 within the research project MU35 "Characterization of crack initiation and propagation in anisotropic material". This research project has been a part of the research activities within the National Centre of Excellence CHARMEC (Chalmers Railway Mechanics). Parts of the funding was provided by the European Union's Horizon 2020 research and innovation programme in the projects In2Track2 and In2Track3 under grant agreements Nos 826255 and 101012456 and in the Europe Rail project IAM4RAIL under grant agreement No. 101101966. The project was carried out under supervision of Professor Johan Ahlström.

Acknowledgements

I would like to thank my supervisor Johan Ahlström for the generous support, encouragement and guidance during the last five years. You are a good friend and I appreciate that you have always been available for a casual conversation or discussion. I am very thankful for being given the opportunity to be the PhD student of this thesis project. I would also like to express my gratitude to my co-supervisor Magnus Ekh, thank you for the valuable discussions and for being a good friend. To Knut Andreas Meyer, I have appreciated working with you and I would like to thank you for all the help and for being a good friend. And to my examiner Christer Persson, you are a funny guy and I have enjoyed our casual conversations. A special thank you to my colleagues and friends for creating an enjoyable and supportive working environment. To my friends from Arvika and to my friend from Brålanda, thank you for being around and I enjoy spending time with you. Last but not least, I would like to thank my girlfriend and best friend Erica, thank you for all your love and support.

Thesis

This thesis consists of an extended summary and the following appended papers:

Paper A D.Gren, J.Ahlström. Fatigue crack propagation on uniaxial loading of biaxially pre-deformed rail steel. *Metals* **13**.10 (2023)

Paper B D.Gren, K.A.Meyer. Effects of predeformation on torsional fatigue in R260 rail steel. *International Journal of Fatigue.* **179** (2024)

Paper C D.Gren, J.Ahlström, M.Ekh. Fatigue crack characteristics in gradient predeformed pearlitic steel under multiaxial loading. *Under review for international publication*

Paper D D.Gren, J.Ahlström, E.Ghassemali, C.Persson. In situ - uniaxial fatigue crack propagation of biaxially pre-deformed pearlitic rail steel *Manuscript*

Paper E K.A.Meyer, D.Gren, J.Ahlström, A.Ekberg. A method for in-field railhead crack detection using digital image correlation. *International Journal of Rail Transportation.* **10**.6 (2022)

The appended papers were prepared in collaboration with the co-authors. The author of this thesis has contributed as follows: **Paper A**, responsible for the major progress of the work i.e., planning of the paper, experimental work, interpretation of results, and writing. **Paper B**, the planning of the work, interpretation of the results, and writing were done together with Dr. Knut Andreas Meyer. The author of this thesis was responsible for the major progress of the experimental work and writing the original draft. **Paper C**, The author of this thesis is responsible for the major progress of the work i.e., planning of the paper, experimental work, interpretation of results, and writing. **Paper D**, the author of this thesis is responsible for the major progress of the work i.e., planning of the paper, interpretation of results, and writing. **Paper E**, the author of this thesis took part in the experimental work as well as review and editing. The major part of the work was done by Dr. Knut Andreas Meyer.

Contents

Chapter 1

Introduction

1.1 Motivation

The impacts from global warming and climate change will continue to increase as the global greenhouse gas emissions reaches new peak levels every year. The consequences of this development must not be underestimated. In order to meet our needs in the near and long term, we must move towards a climate-neutral society. This is a great challenge which involves every sector of society, and not least the transportation sector. Transportation alone stood for 16.2 % of the CO_2 emissions in 2016 [1] and reducing the emissions to net-zero is therefore of great significance. The need of energy efficient and climate neutral means of transportation makes rail transportation a good candidate. Rail transportation is one of the most energy efficient and safest modes of transportation. It has the potential to play an important role in the net-zero transition. However, this is provided that safety, functionality and reliability as well as economic feasibility can be ensured. The major material related challenge is rolling contact fatigue which impairs safety and reliability as well as the economic feasibility. Understanding how the mechanical behavior and material properties in wheels and rails change in service and how this evolution effect crack initiation and crack propagation is one key factor to mitigate the effect of rolling contact fatigue.

The area of the contact patch between the railway rail and wheel has the size of a small coin and axial loads between 6-12 tonnes are typical static levels. Thus the contact stress becomes very high. In addition to axial load, the rail is also subjected to frictional forces resulting from traction, cornering and flange contact. The frictional forces can cause the surface material to become severely deformed. The microstructure of the severely deformed material is aligned and the mechanical behavior is anisotropic. It is well known that many defects associated with rolling contact fatigue is initiated at the severely deformed surface. However, the material properties and mechanical behavior of the severely deformed surface material is not fully understood.

Previous projects (M24, MU27, MU28, MU34) conducted within the research group Chalmers Railway Mechanics (CHARMEC) have investigated the severely deformed surface material. A predeformation method for replicating the material state close to the surface of deformed rail was developed. The microstructure, yield surface and local strength was characterized and the evolution of anisotropy with predeformation modelled. This project is a continuation of the previous work and is focused on the effect of anisotropy on fatigue crack initiation and propagation.

1.2 Aim and scope of research

The background to this thesis work is the changes in mechanical properties and fracture characteristics of the railhead surface layer induced by rolling contact fatigue loading. The material properties are locally changed by plastic deformation, work hardening, residual stresses and generation of anisotropy. In addition, thermal effects due to breaking and traction induce changes in the local material properties, although these effects are not within the scope of this thesis. A fundamental understanding of the changes in mechanical behaviour and material properties of the severely deformed surface material of rail heads is a key factor in mitigating the detrimental effects of rolling contact fatigue. Consequently, by understanding when cracks are likely to form and the subsequent crack growth behaviour, it will be possible to improve maintenance guidelines to increase the safety, viability and reliability of the railway system.

This thesis examines the fatigue crack behaviour of anisotropic pearlitic rail steel, focusing in particular on the rail grade R260. In order to investigate the influence of anisotropy on fatigue crack behaviour, a pre-deformation method was employed to replicate the material state of the surface material of severely deformed railheads. This forms the basis for the experimental work presented in this thesis. The aim of this thesis work is to better understand how the anisotropy developing in service of railway rails changes the fatigue crack behavior. The aim was approached by investigating the relation between crack propagation, crack path and degree of anisotropy under different loading conditions. The work presented in this thesis consists of five appended papers with the following scope:

- **Paper A**: Uniaxial fatigue crack propagation of predeformed rail material. In this study the effect of large shear deformation on the crack direction and crack propagation rate was investigated.
- **Paper B**: Fatigue crack propagation under pulsating torsional cyclic loading. In this study, a method for fatigue life evaluation of deformed material under loading conditions similar to rolling contact loading was proposed. The effect of predeformation on crack growth direction and number of cycles to failure with respect to the direction of torsional load and superimposed axial load was investigated.
- **Paper C**: Fatigue crack propagation under non-proportional multiaxial loading. In this study, the effect of predeformation on crack propagation, crack path and fatigue behavior was investigated.
- **Paper D**: In-situ uniaxial fatigue crack propagation. In this study, single edge notched specimens were machined from predeformed test bars along two directions. The effect of microstructure orientation on the crack growth behavior was examined and compared with undeformed material.
- **Paper E**: A method for in-field railhead crack detection using digital image correlation was proposed. The method was evaluated under laboratory conditions by four point bending of a used rail section. The crack network of the rail section was investigated by serial sectioning and connected to the DIC results.

Chapter 2

Theory

2.1 Railway-wheel

The geometry of a typical rail-wheel interface is shown in Figure 2.1. On straight tracks or in large radius curves, the running surface of the wheel and the railhead are in contact. This is the least severe contact between the rail and the wheel, resulting in the lowest contact stresses and lateral forces. In tighter curves, however, the contact condition becomes much more severe as the wheel flange comes into contact with the gauge corner of the rail. This is the wheel/rail contact responsible for the severely deformed surface material commonly observed in the near-surface region of the gauge corner [2]. The load condition, as described above, depends on the wheel-rail contact. This contact varies along the rail and over time as the geometry of the rail and the wheel profile changes due to wear and plastic deformation. In addition, various factors such as train type, acceleration, speed and weather conditions affect the loading condition. As the associated material damage is dependent on the load history, it becomes difficult to evaluate and fully understand, the degradation mechanisms studtying field samples alone.

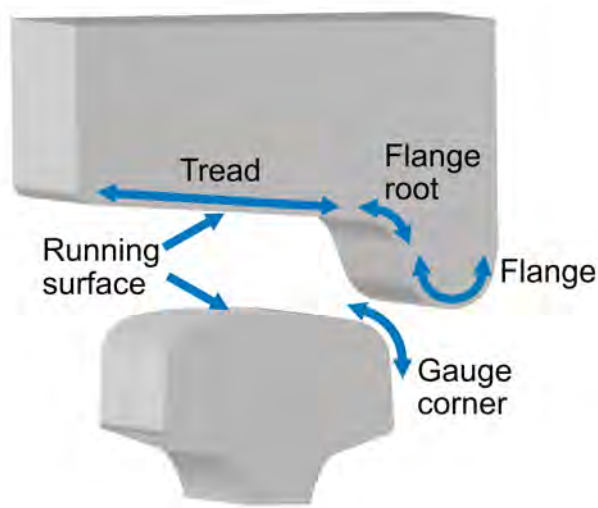

Figure 2.1: Geometry of a typical wheel-rail interface.

2.2 Pearlite morphology

Pearlitic steels have a two-phase microstructure comprising alternating lamellae of ferrite and cementite. Pearlite forms through an eutectoid reaction where austenite transforms into ferrite and cementite. The morphology of the pearlitic microstructure is illustrated in Figure 2.2. The nodules are formed on the boundaries of prior austenite grains through the growth of pearlite colonies. The nodules are composed of several differently oriented colonies [3], where each colony is characterised by similarly oriented lamellae of ferrite and cementite, with semi-coherent lamellae boundaries [4].

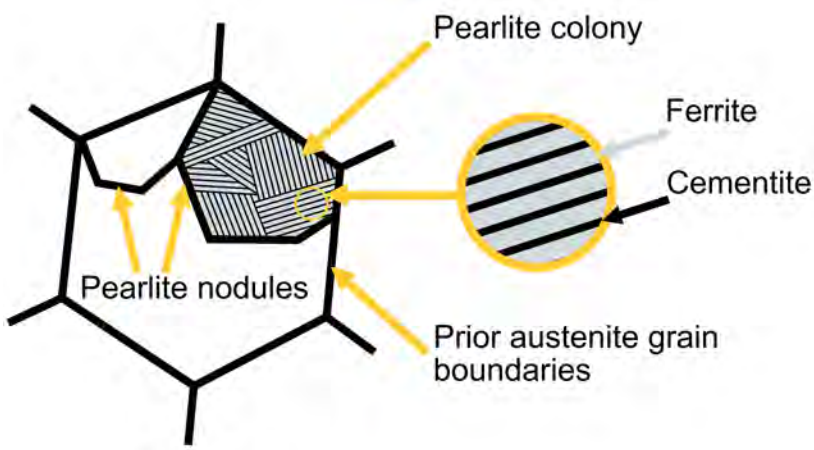

Figure 2.2: Morphology of the pearlitic microstructure.

The formation of pearlite from austenite can be achieved through either continuous cooling or isothermal cooling. The interlamellar spacing, determined by the carbon diffusion rate, can be tailored with both methods [5]. In isothermal cooling, the interlamellar spacing is controlled by the degree of undercooling, where a decrease in holding temperature results in a decrease in the interlamellar spacing. Similarly, an increase in the cooling rate during continuous cooling results in a decrease in the interlamellar spacing [6]. The time temperature transformation (TTT) diagram and continuous cooling transformation diagrams (CCT) respectively describe the interval in which pearlite is formed.

2.3 Crack initiation and crack propagation

2.3.1 Crack propagation modes

Cracks can propagate under different loading modes, either by a combination of the three basic loading modes shown in Figure 2.3 or by only one of these modes. When combining loading modes, it is referred to as mixed mode loading. Conversely, if only one mode is present, it is called single mode loading. Mode I loading, also known as opening mode, occurs when the crack is loaded in tension perpendicular to its plane, causing the crack surfaces to pull apart. Most cracks in engineering structures propagate under mode I loading. Crack propagation under shear loading is referred to as Mode II or Mode III, depending on the orientation of the shear load relative to the crack plane. Mode II is the shear mode, which occurs when the applied shear load is parallel to the crack plane and the crack front is perpendicular to the applied shear load. In this case, the crack faces slide over each other. Mode III is known as the tearing mode. In this case, the crack front is parallel to the applied shear load, and the crack propagates by tearing along the direction of the applied force [7], [8].

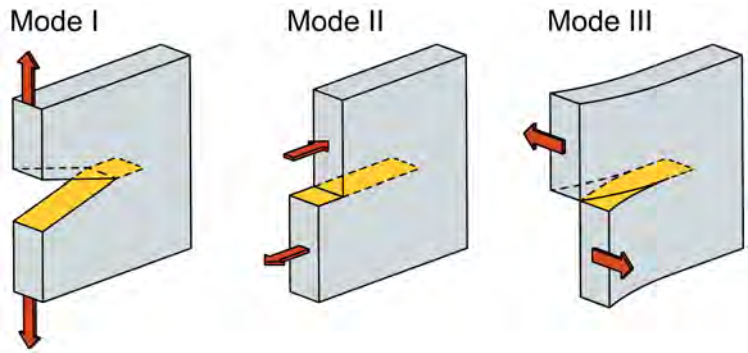

Figure 2.3: Three modes of crack propagation.

2.3.2 Rolling contact fatigue

Rolling contact fatigue is the process of crack initiation and propagation in materials subjected to repeated rolling contact, commonly observed in applications such as gears, roller bearings, railway rails, and wheels. It's important to note that fatigue crack propagation due to rolling contact fatigue differs from classical fatigue, as cracks predominantly grow under compressive loads. At the rail-wheel contact, stresses are generated by the wheel load and frictional forces caused by traction, cornering, and braking. The imposed loading conditions induce a multiaxial and non-proportional stress states [9], dependent on various factors such as the size and location of the contact patch, magnitude of loads and surface condition [10]. Typically, crack initiation is preceded by plastic deformation, and the load history of the material determines the propensity for crack initiation, the number of cracks initiated, their location, and the angle of crack initiation [11, 12, 13].

Examples of different types of rolling contact fatigue cracks are shown in Figure 2.4. These cracks can be either surface or subsurface initiated. Figure 2.4a shows a subsurface-initiated crack caused by a vertical load on a rolling object, inducing shear stress below the surface [14]. Such subsurface-initiated cracks are typically associated with material defects such as manganese sulphides (MnS). In addition, the rolling contact loading in Figure 2.4a can lead to a surface-initiated crack in the presence of a surface asperity, as shown in Figure 2.4c. Surface asperities act as stress raisers, promoting crack initiation.

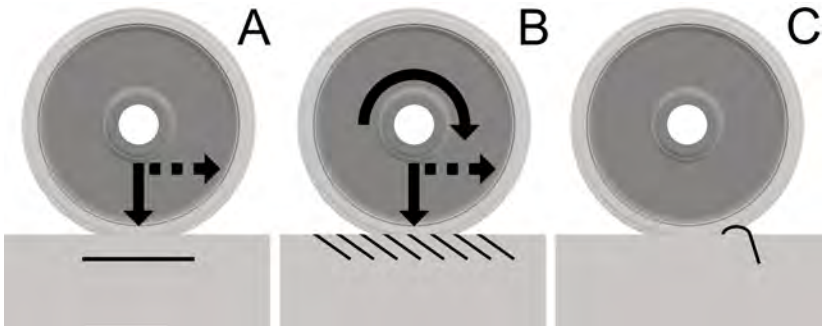

Figure 2.4: Examples of rolling contact fatigue cracks, modified from [14].

The most commonly observed rolling contact fatigue cracks in rails are called head checks, as shown in Figure 2.4b and Figure 2.5, other examples of rail defects can be found in the comprehensive review of [15]. Head checks are formed when the rail is subjected to both vertical and shear loads. The shear loads cause severe plastic deformation when the magnitude of the interfacial shear stresses from traction, cornering and braking repeatedly exceeds the yield strength. This becomes most severe in unidirectional traffic when the wheel flange is in contact with the gauge corner of the rail [9]. As a result, shear strains accumulate (ratchetting), causing hardening and alignment of ferrite and cementite lamellae in pearlitic steels [16], [17]. Crack initiation occurs when the fracture strain is exceeded and subsequent crack growth occurs along direction of the microstructure alignment [18]. These cracks grow mainly under mixed mode II and III loading, as mode I propagation is suppressed by the compressive stress in the contact zone. As the crack grows deeper, into the undeformed material and out of the contact zone, crack growth is diverted to mode I growth. The crack can then propagate either downwards or upwards depending on the weakest path and the bulk stresses (residual, bending and thermal stresses) depending on the stress state. The rate of mixed mode crack propagation depends on the crack surface friction. Increasing friction reduces the rate of crack propagation. Therefore, lubrication increases crack propagation. However, lubricating rails reduces the risk of crack initiation [9],[8].

Figure 2.5: Head checks on the gauge corner of the rail.

2.4 Anisotropy

2.4.1 Methods for producing anisotropic pearlitic steel

Anisotropy refers to the direction dependent physical properties of a material, e.g. the direction dependent strength. When pearlitic steels are severely deformed, they can exhibit a crystallographic texture and shear bands resulting in anisotropic mechanical properties. For example, surface region of rails exhibits anisotropic properties due to the large accumulation of plastic shear strain. Several processing techniques are available to produce severely deformed pearlitic steels. The most common method is wire drawing, which produces a microstructure in which the ferrite and cementite lamellae are aligned along the drawing direction [19] and [20]. Using this method, pearlitic steels can achieve yield strengths of up to 6 GPa [Source]. However, the loading imposed by wire drawing is very different from the loading conditions at wheel-rail contact. A processing technique where the applied load is very similar to wheel-rail contact is High Pressure Torsion (HPT), where the material is deformed by large shear strains under the application of large compressive hydrostatic stresses, see e.g. [19] and [20]. This method makes it possible to produce a material condition similar to the highly deformed surface material of rails. The severe deformation of the material is made possible by the high hydrostatic pressure, which suppresses crack initiation and propagation i.e. the fracture strain is significantly increased by the compressive stress. From a railway perspective, it is of particular interest to study the evolution of the microstructure and mechanical properties of pearlitic steels subjected to high pressure torsion.

2.4.2 Evolution of microstructure alignment

The microstructure of pearlitic steels aligns along the direction of the applied load when subjected to medium and large strains. The deformation also cause thinning of the lamellae i.e., a decrease in interlamellar spacing. At very high strains the lamellae in wires becomes parallel to the drawing direction and in high pressure torsion parallel to the shear direction [21], [19]. The high straining also leads to dissolution of cementite [22].

At the microscopic scale the alignment is not perfect. The reorientation of the cementite lamellae is dependent on initial orientation with respect to the load axis. Unfavorable orientation cause the cementite lamellae to bend and fracture [21],[22],[23]. Wavy and fragmented lamellae are commonly observed in the surface layer of rails subjected to severe deformation, see e.g. [24],[25],[26].

2.4.3 Mechanical properties of anisotropic pearlitic steel

Fracture toughness and fatigue crack propagation rate have been found to be a strong function of the ferrite-cementite orientation. The fracture toughness of pearlitic steels deformed with high pressure torsion is dependent on the relative orientation between the crack plane and cementite lamellae. Crack plane oriented parallel to cementite lamellae exhibit the lowest fracture toughness, lower than for undeformed pearlite. The fracture toughness on the other hand increase for crack planes perpendicular to the cementite lamellae [19],[20]. The observed anisotropy is attributed to the lamellae alignment. The fatigue crack propagation rate follows the same trend where an increase in crack propagation rate is observed for crack planes oriented parallel to the cementite lamellae. The trend was observed for equivalent von Mises strains of 2 and upwards [27], [28].

2.5 Strength of pearlite

2.5.1 Yield strength

The yield strength of undeformed pearlitic steels is primarily controlled by the interlamellar spacing. The strong influence of the interlamellar spacing have been explained on the basis of an effective slip distance [6], [29], [30]. Dislocations cannot easily continue their movement through the cementite lamellae and thus the interlamellar spacing controls the available slip distance. Thus, a decrease in interlamellar spacing increases the yield strength as it becomes more difficult to move the dislocations upon macro-yielding. The explanation is based on the assumption that dislocation sources becomes activated in a micro-yield region at the ferrite-cementite interface i.e. dislocations are generated at low strains prior macro-yielding. The assumption of activated dislocations sources at the ferrite-cementite interface have been proven to be valid by transmission electron microscopy. According to Dollar et al [30], microyielding could be explained by incompatibility strains between the ferrite and cementite lamellae. The yield strength of pearlitic steels can be approximated with equation (1) which is a Hall-Petch equation type equation with respect to the interlamellar spacing. The equation have been established through regression analysis.

$$\sigma_y = \sigma_0 + \frac{k_y}{\sqrt{S}} \tag{2.1}$$

Where σ_{y} is the resulting yield stress. The interlamellar spacing is denoted by S and the material constants k_y and σ_0 reflects the lattice friction stress and dislocation locking (contribution of from work hardening) respectively.

Additional strengthening mechanisms contribute to the yield strength of deformed pearlite. Zhang [21] investigated the evolution of yield strength in cold drawn pearlitic wires by successive straining. Microstructural analysis identified three strengthening mechanisms that contribute to the observed yield strength with strain, namely: grain boundary strengthening, dislocation hardening and solid solution hardening. The yield strength could successfully be estimated by linear addition of the individual contributions for the investigated range of drawing strain. The solid solutions strengthening mechanism is based on cementite dissolution causing carbon enrichment of ferrite. Cementite dissolution have been observed in severely deformed pearlitic steels. The grain boundary strengthening is based on the interlamellar spacing which decrease with drawing strain and act as barrier for dislocation movement. Dislocation strengthening is based on dislocation entanglement which increase with dislocation density. A similar study was conducted by Nikas et al [31] for pearlitic rail steel deformed by torsion under compression. The increase of yield strength with shear strain was attributed to dislocation hardening and grain boundary hardening.

2.5.2 Work hardening

Plastic deformation of pearlitic steels is inhomogeneous owing to differences in mechanical properties of the two phases (ferrite and cementite) and differences in the orientation of nodules and lamellae throughout the structure. Internal stresses denoted according to its origin namely phase stress, block (nodule) stress and colony stress are thus generated upon plastic deformation [32]. In-situ neutron diffraction of pearlitic steels during tensile deformation have confirmed this strain inhomogeneity [32, 33, 34, 35, 36, 37]. The elastic strain of the constituent phases of undeformed pearlite remained equal up to the onset of macro-yielding as the elastic moduli are similar. The yield stress of cementite is considerably higher than that of ferrite which cause stress partitioning at the onset of yielding. It was found that this stress partitioning is the governing mechanisms for the high work-hardening observed in undeformed pearlitic steels. The cementite is mainly elastically deformed whilst the ferrite phase is plastically deformed. The average stress in the structure could be approximated with a rule of mixtures based on the volume fraction of cementite and the measured elastic strain in each respective phase [37]. The degree of work hardening was found to be independent of interlamellar spacing and prior dislocation density. In conclusion, the yield stress is governed by the hardness of ferrite which depend on solid solution strengthening, dislocation hardening and interlamellar spacing but the increase in dislocation density during plastic deformation does not significantly affect the degree of work hardening [34].

2.6 Predeformation - Replication

Understanding the material properties and mechanical behavior of the severely deformed surface layer requires extensive mechanical testing and material characterization. However, in practice the material state is very difficult to evaluate. The difficulties originate from the high and non-linear strain gradient present in the severely deformed surface layer. Moreover the surface layer is very thin and the degree of plastic deformation varies along the rail. Thus, if test bars of reasonable size were to be extracted the material state would be heterogeneous and difficult to replicate.

The material state can be replicated through the application of hydrostatic compressive stress and shear stress. Equal angular channel pressing, and high-pressure torsion are two severe plastic deformation techniques that have been used previously in research to replicate the severely deformed surface layer [19, 20, 27, 28, 38]. These methods can achieve shear strain magnitudes similar to that of field samples. However, the size of the samples that can be extracted is very limited making it difficult to achieve axi-symmetrical specimens which are required for multiaxial axial-torsion fatigue testing.

Meyer [39, 16] developed a method capable of replicating the material state in axi-symmetric test bars by twisting cylindrical test bars under a constant compressive load. This method can achieve shear strains up to 2.3 in standard test bars with 10 mm diameter gauge. The material state was shown to be representative for the material state in the severely deformed layer with equal amount of shear strain. The microstructure obtained with this method is shown in Figure 2.6. The main drawback with this method is that shear strains at a level as high as found the very top surface of the rails cannot be achieved.

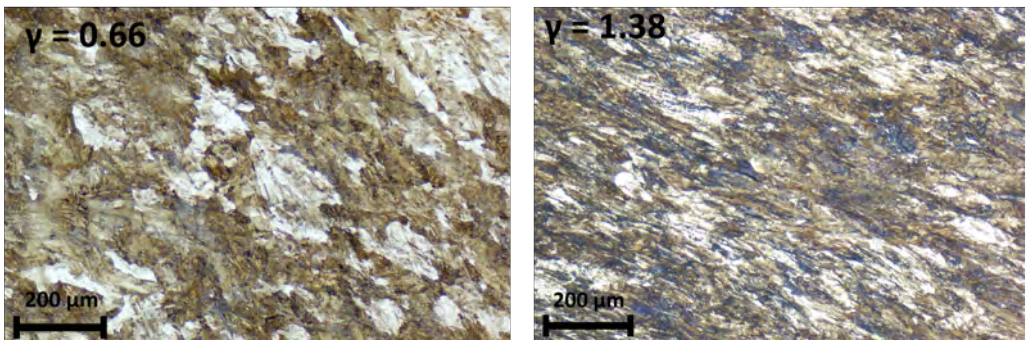

Figure 2.6: Microstructure obtained by predeforming axi-symmetric test bars through torsion under a constant compressive load.

2.7 Dislocation theory

Plastic deformation is defined as permanent deformation. In metals, plastic deformation occurs by slip facilitated by dislocation movement and/or twinning. The deformation mechanism in pearlitic steels is restricted to slip which can be defined as the relative movement between two atomic planes by the motion of dislocations. Dislocations are line defects and exists in all polycrystalline materials. There are two basic types, edge dislocations and screw dislocations. In general, dislocations are mixed, having the character of both edge and screw. Movement of dislocations requires an imposed shear stress of a certain magnitude which is dependent on the microstructure and crystal structure and orientation as well as the dislocation density and composition [40].

The ideal slip process with an edge dislocation, starting off from an initial perfect 3-dimensional lattice is illustrated (in two dimensions for a simple cubic crystal structure) in Figure 2.7. The applied shear stress breaks the lattice and introduce the dislocation in Figure 5b. The edge dislocation is seen as an extra atomic half plane. Dislocation movement through the lattice (Figure 2.7c-f) occurs under the application of an applied shear stress by breaking the bonds connecting the lower half plane to the neighboring lattice plane. Thus, the dislocation is moved by shifting its position i.e. the atoms of the dislocation in Figure 2.7b and Figure 2.7c are not the same. The slip step is produced in Figure 2.7e as the dislocation reached a free surface [40].

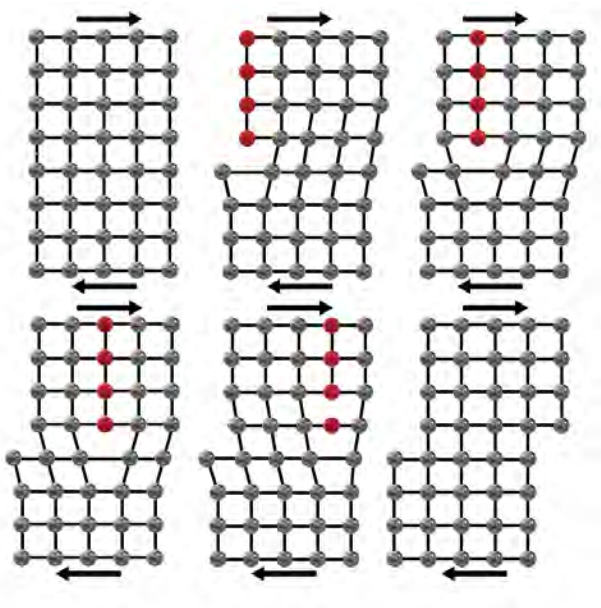

Figure 2.7: Illustration of deformation by slip with an edge dislocation.

Dislocations can only glide along specific crystallographic planes called slip planes an in specific directions called slip directions. In general slip planes are the most dense planes and the slip direction is the most closed packed direction. The active slip plane is in general the plane with the highest resolved shear stress. However, slip in body center cubic (bcc) metals such as pearlitic steels is anomalous. In bcc metals, there exist only one close packed direction but no closed packed planes. The slip direction is $< 111 >$ and the most dense planes are $\{110\}$, $\{112\}$ and $\{123\}$ which all have the same density. The most common slip plane in iron is $\{110\}$ and three of these planes intersect along the $< 111 >$ direction. The intersection makes it possible for cross-slip and therefore slip is often not well defined but wavy. Moreover, the active slip plane/s within the slip system is dependent on composition, crystal orientation, temperature and strain rate [40].

Chapter 3

Mechanical testing

3.1 Predeformation - Replication of anisotropic rail surface material

Replication of the material state found close to the surface of highly deformed railheads forms the basis of this thesis work. The material state was replicated by using the predeformation method developed by Meyer in [39]. With this method, solid cylindrical test bars are repeatedly twisted 90° under a constant compressive force, as described and illustrated in figure 3.1a. Test bars subjected to the predeformation process undergo geometry changes, manifested as a diameter increase and shortening of the gauge section. Reprofiling is required before predeformed test bars can be used for fatigue testing because such test bars needs to be axi-symmetric and have a well defined geometry.

In this thesis work, solid cylindrical test bars with an initial gauge section diameter of 10 mm was used. The constant compressive force was set to give an initial nominal compressive stress of 500 MPa to prevent buckling and avoid premature failure during predeformation. After predeformation, the test bars were reprofiled and polished followed by machining a notch. In total, three different predeformation levels have been investigated in this thesis work, denoted as PD1, PD3 and PD6. PD is the abbreviation for predeformation and the number stands for number of twisting cycles i.e., PD1 corresponds to twisting 1x90°.

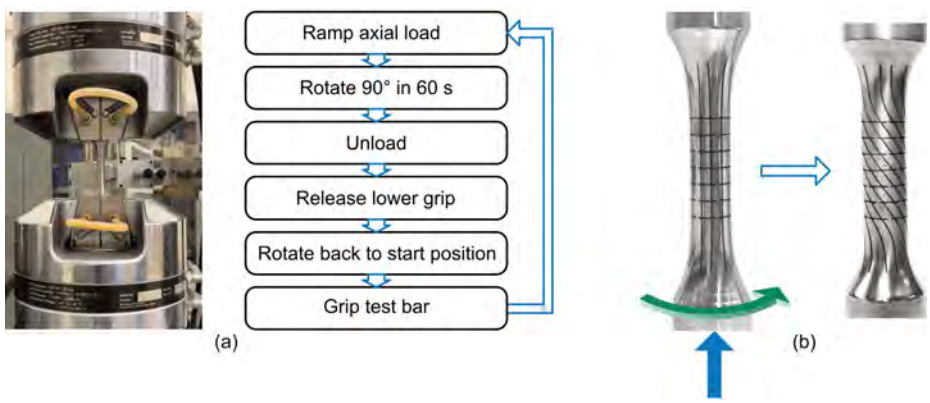

Figure 3.1: Predeformation method. (a) flowchart of the predeformation process and (b) visualization of shear deformation resulting from twisting 3x90°.

In **Paper A**, a laser etched grid was imprinted prior predeformation to facilitate the assessment of accumulated shear deformation on the surface. Figure 3.1b illustrates the laser etched grid prior and after predeformation to PD3. The shear deformation at the surface was quantified by calculating the surface shear strain γ, as follows:

$$\gamma = tan(90 - \alpha) \tag{3.1}$$

where α is the angle measured between the intersecting lines of the deformed grid, as shown in Figure 3.2.

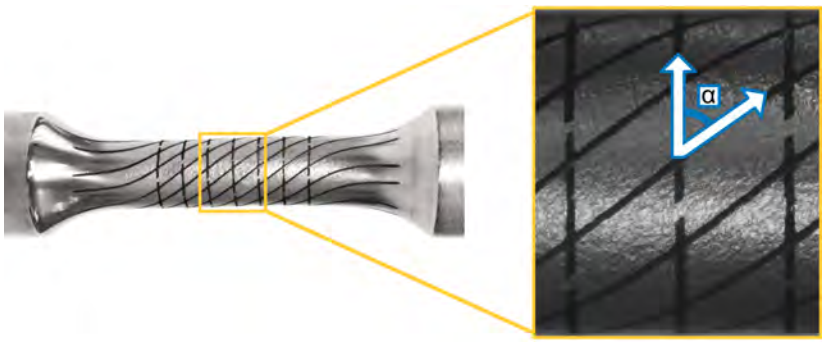

Figure 3.2: Shear strain measurement of predeformed test bars.

To ensure a robust sample size, α was measured at 24 locations, evenly distributed around the circumference of the gauge section. Each test bar was rotated in increments of 60°; at each rotation, the angle was measured at four locations along the center line to minimize the influence of test bar curvature. A total of 20 test bars were measured, 10 for each predeformation state (PD3 and PD6).

3.2 Hardness measurement

The deformation gradient in the predeformed test bars was characterized by determining the hardness distribution using the Vickers method. This characterization was done in **Paper A** were the hardness distribution was measured on the preformed material states PD3 and PD6 along with undeformed material as reference hardness. Hardness was measured along the axial cross-section for the gauge section, according to the indentation pattern shown in 3.3. The samples for hardness measurements were extracted after reprofiling and fatigue testing. To avoid influence of plastic deformation caused by the stress concentration around the notch and the growing crack, the samples were cut out 2 mm from the top of the hole that forms the notch. To verify that the hardness measurements of samples were unaffected by the fatigue crack propagation experiments a reference sample from a reprofiled PD6 test bar was extracted. The applied load was 5 kgf (HV5) for all measurements to enable comparison between the samples without risking the possible size effect. The equipment used for conducting the hardness measurements was the hardness tester DuraScan 70 G5 from Struers/Emcotest.

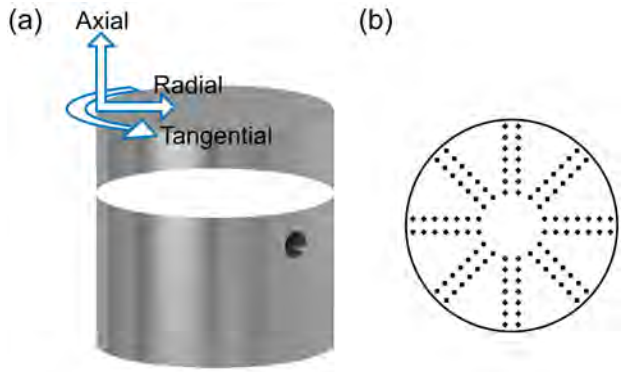

Figure 3.3: Illustration of the hardness pattern used for characterizing the hardness gradient.

In **Paper C**, the deformation caused by out of phase biaxial fatigue loading was studied by measuring the change in hardness. The hardness measurements were made on the axial-cross section, close to the fracture surface, according to the indentation pattern shown in figure 3.3. The hardness map constitutes of two parts, one showing the hardness distribution close to the residual fracture and the other close to the fatigue zone. Characterization of the hardness distribution is important in the interpretation of the mechanical behavior as the recorded force/torque response only shows the average mechanical behavior. The hardness measurements from **Paper A** was used as reference hardness.

3.3 Digital image correlation

Digital Image Correlation (DIC) is an optical measurement method that allows one to determine a surface displacement field. Deriving from this the surface strain field provides in-depth insight into material deformation. The principle of measurement is pattern recognition, which means that a random speckle pattern is applied to the surface—preferably over a white background with black speckles to generate good contrast. A reference image is taken, which is typically done in the unloaded state, and then a series of images are captured under load. To determine the displacement field, the region of interest is divided into a mesh of subsets. With the reference image, it is possible to track how these subsets deform during loading. This is done by searching for matching subsets in the deformed image. By using a correlation criterion which evaluates the difference between two subsets, the subset with the highest probability to correspond to the subset in the reference image can be found. A larger subset has more uniqueness, and hence better correlation can be achieved. However, fewer data points are tracked resulting in lower spatial resolution. In addition to the subset size, the distance between each subset called step size also affects the spatial resolution but less than the subset size. The accuracy is dependent on numerous factors including quality of speckle pattern, pattern recognition and lightning. For detailed description of DIC measurement, see Sutton et al [41].

3.4 Mechanical testing

3.4.1 Paper A - Uniaxial fatigue crack propagation

In **Paper A**, uniaxial fatigue crack propagation experiments were conducted on pearlitic rail steel R260, examining both undeformed (PD0) and predeformed (PD3 and PD6) material state to investigate the effect of predeformation on the crack propagation behavior. The experiments were load controlled, using a sinusoidal load waveform at a frequency of 10 Hz. Two nominal stress amplitudes with zero mean stress were employed, corresponding to 60% and 70% of the offset yield strength in tension for undeformed material. The offset yield strength $Rp_{0.2}$ was measured in a previous study by Meyer et al. [39] to 534.2 MPa, on samples from the same material batch. A total of three test bars of each type were tested, i.e. a total of 18 test bars.

The test bars used in this study were mirror polished and notched before fatigue testing. A drilled holed served as a starting notch to create a stress concentration to steer crack initiation, see 3.4 for notch and test bar geometry. The fatigue experiments continued until failure and the equipment used for fatigue testing was the servo-hydraulic axial-torsion system MTS 809, equipped with a ±100 kN and ±1100 Nm load cell.

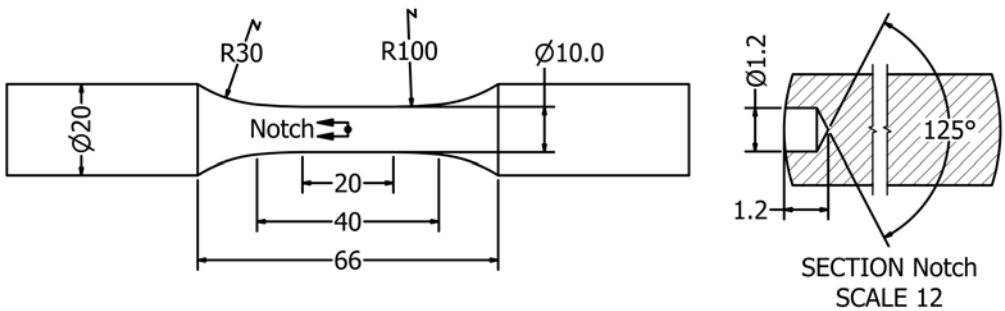

Figure 3.4: Dimensions and geometry of the notched test bars used in **Paper A**. Dimensions in mm.

Micrographs of the surface crack were acquired using both stereo- and optical microscope. Each micrograph represents the projection on the image plane as seen in figure 3.5. The crack width was measured on stitched images and corrected for the curvature of the test bar.

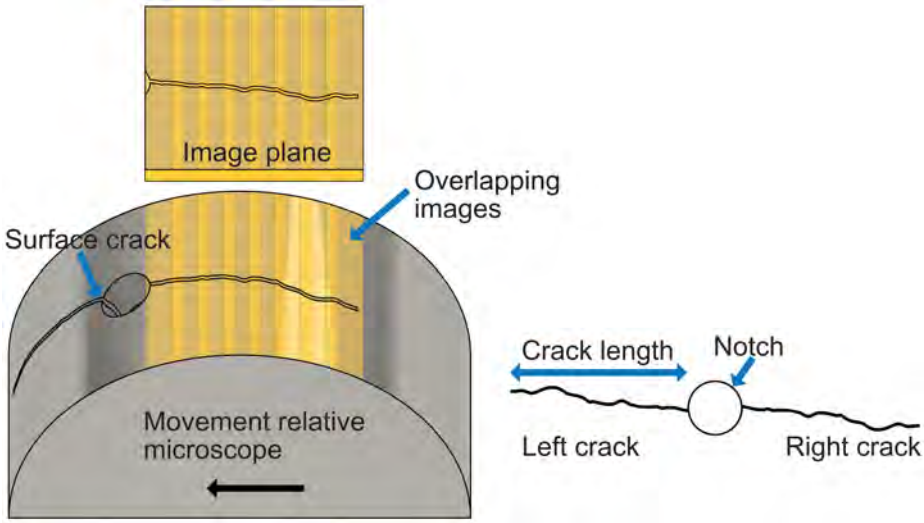

Figure 3.5: Illustration of crack measurement with stereo and optical microscope in **Paper A**.

3.4.2 Paper B - Torsional fatigue crack propagation

In **Paper C**, fatigue crack propagation experiments under pulsating cyclic loading were conducted on both undeformed (PD0) and predeformed material (PD3) to study the influence of load direction on the fatigue behavior of predeformed material. The fatigue experiments were strain controlled to avoid ratchetting. The torsional strain was controlled by the rotation angle $\theta = 0.0132 \pm 0.0044$ [rad], measured with a biaxial extensometer (MTS 632.80F, 1.2/-0.5 mm, $\pm 5^{\circ}$) over its gauge length, as depicted in Figure 3.6. The strain interval was experimentally determined to achieve an initial torque response of 0 to 50 Nm for undeformed material. This loading gives a maximum elastic shear stress range about 850 MPa at the notch root and elastic shear strain of about 0.01, as shown by the Finite Element simulation results in Fig. 5. The waveform of the torsional load was sinusoidal and the test frequency was set to 1 Hz.

The test matrix for the fatigue experiments is shown in table 3.1. The torsional load was either applied along or against the direction of predeformation, with or without a superimposed compressive axial load of -100 MPa. Axial and torsional stiffness were measured every 1000th cycle and was used as a measure of the material damage evolution during testing. The fatigue life was defined as the number of cycles until a 5% drop from the initial axial stiffness. The test bars used in this study had a circumferential notch with a notch radius of 0.4 mm, see figure 3.6. The machine used for the fatigue experiments was the servo-hydraulic axial-torsion system MTS 809.

Table 3.1: Test matrix.

Predeformation	Direction	Axial load	Nr of test bars
PD0	Along	-100 MPa	3
PD0	Along	0 MPa	3
PD3	Along	-100 MPa	2
PD3	Along	0 MPa	2
PD3	Against	-100 MPa	1

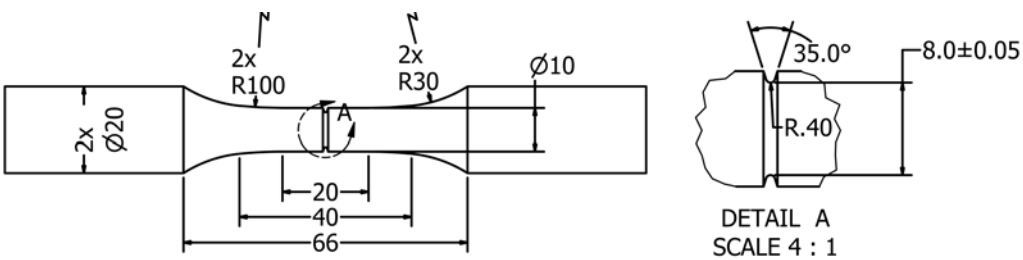

Figure 3.6: Geometry and dimensions of notched test bars in **Paper B** and illustration of the measured rotation angle θ. Dimensions in mm.

The stiffness measurement procedure is described in figure 3.7. The figure shows three measurement intervals in which the measured quantities are time averaged to reduce influence of measurement noise. The measured quantities were torque (T), rotation angle (θ), axial force (F) and axial strain (ϵ). Torque and rotation angle was used to calculate torsional stiffness according to equation (3.2). Similarly, axial force and axial strain was used to calculate axial stiffness according to equation (3.3). Torsional stiffness was measured under an axial load of 50 MPa to reduce the influence of crack face contact and axial stiffness was measured in unloading between 50 MPa and 20 MPa to reduce influence of plasticity and closing cracks.

$$\text{Torsional stiffness} = \text{abs}\left(\frac{T_1 - T_2}{\theta_1 - \theta_2}\right) \tag{3.2}$$

$$\text{Axial stiffness} = \text{abs}\left(\frac{F_1 - F_2}{\epsilon_1 - \epsilon_2}\right) \tag{3.3}$$

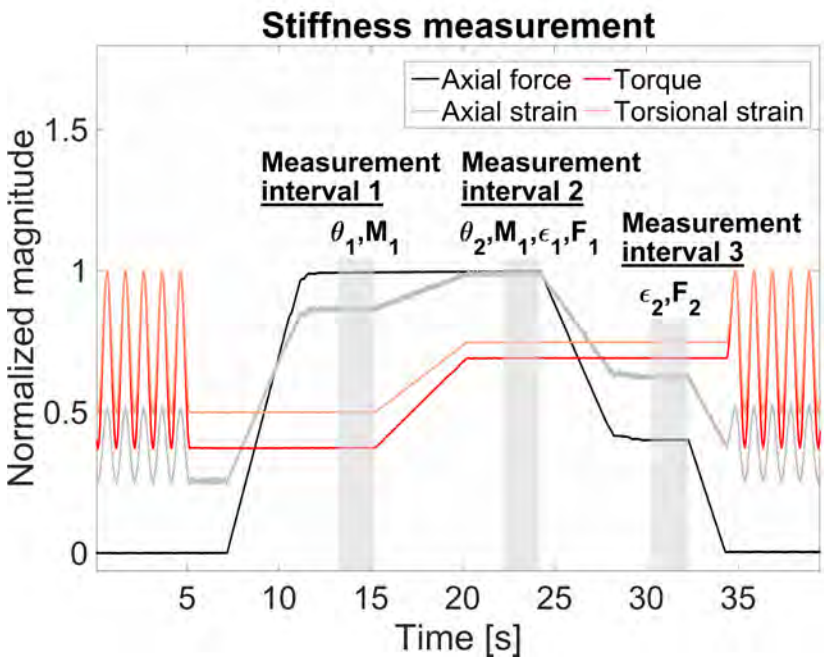

Figure 3.7: Measurement of axial and torsional stiffness in **Paper B**.

3.4.3 Paper C - Non proportional multiaxial fatigue crack propagation

In **Paper C**, fatigue crack propagation (FCG) experiments were carried out under non-proportional multiaxial fatigue loading with a phase difference of 90°. The aim of this study was to investigate the influence of pre-deformation on the fatigue crack propagation behavior under rolling contact-like conditions. In addition, the low cycle fatigue (LCF) behavior was also investigated. For this purpose, three predeformed material states corresponding to PD1, PD3 and PD6 were investigated together with an undeformed material state of the pearlitic rail steel R260. The geometry of the test bars used for the fatigue crack propagation experiments is shown in Figure 3.8 The same test bar geometry was used for the low cycle fatigue tests, except that no notch was used.

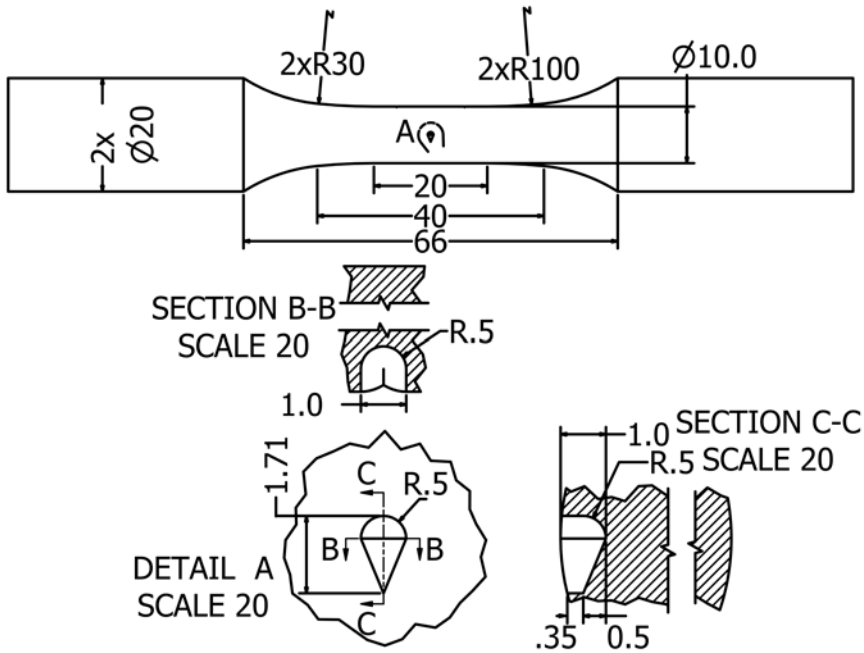

Figure 3.8: Geometry and dimensions for notched test bars used in **Paper C**.

To control crack initiation, special considerations were made in the design of the notch. The notch was designed to achieve the highest stress concentration in the same point for both axial and torsional load. As shown in the 3D illustration of the notch interior in Figure 3.9, the interior is smooth except for the pointed end of the notch. The notch has been machined by spark erosion (EDM) and therefore the tip has a small radius.

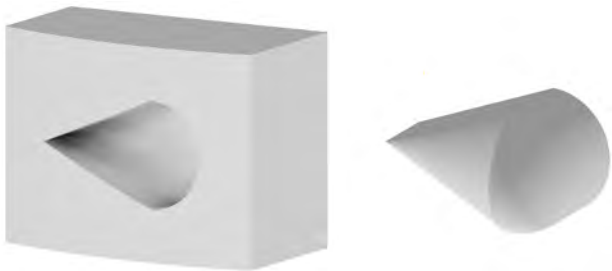

Figure 3.9: Illustration of notch for multiaxial fatigue crack propagation experiments in **Paper C**.

The LCF and FCG experiments were strain controlled and conducted with a nominal equivalent von Mises strain amplitude of 0.6 %. The choice of strain amplitude was based on a previous study by Somrita et al [42] who performed non-proportional multiaxial fatigue experiments on the pearlitic rail grade R350HT. The same strain amplitude was chosen to enable comparison. The axial and torsional strain amplitudes were set to 0.424% and 0.735% respectively, giving a circular strain path in the ϵ vs $\gamma/\sqrt{3}$ strain space, see figure 3.10. The frequency was set at 0.2 Hz to avoid adiabatic heating due to the large plastic strain amplitude and to ensure robust testing (stable PID settings).

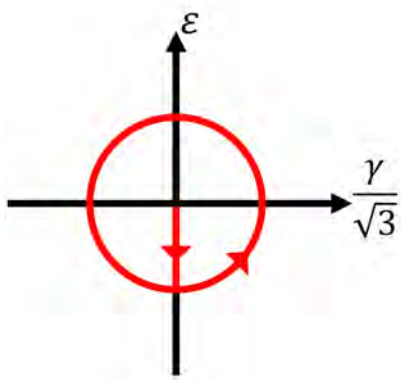

Figure 3.10: Strain path for out of phase multiaxial fatigue loading in **Paper C**

During the fatigue crack propagation experiments, the surface crack length was monitored using a 3D DIC stereo microscope system provided by Correlated Solutions. Images were acquired at a frequency of 2 Hz, corresponding to 10 images per load cycle, to allow crack monitoring of all load cycles. The analog load signals from the axial-torsion machine were recorded simultaneously with the image acquisition. The 2 Hz acquisition rate was chosen to resolve the sinusoidal load wave, including the max/min peak load for both torsional and axial loading. This allowed an image to be taken close to the peak loads for each cycle. The surface crack length measurements were based on images taken close to the maximum axial load where the crack is almost fully open. A Matlab script was written to sort the images by finding the peak loads from the analog load data. The magnification range used for the stereo microscope during the tests was between 0.6 - 1.2x, starting with the highest magnification during early crack growth. The setup is shown in Figure 3.11.

Figure 3.11: Stereo microscope set up for crack measurement and DIC measurement in **Paper C**

The interval for measuring the surface crack length was set to every 16th cycle after the first crack was detected and the surface crack was measured from both sides of the notch. Crack length was defined as the distance from the notch edge to the circumferential position of the crack tip along the surface, regardless of any axial inclination, as illustrated in Figure 3.12

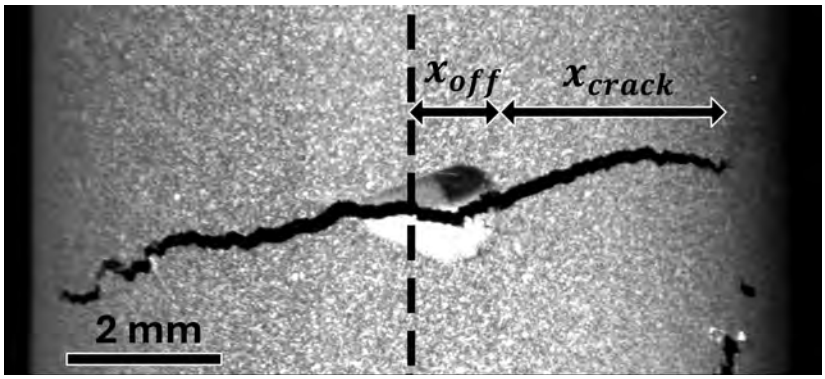

Figure 3.12: Illustration and description of the surface crack length measurements in **Paper C**

As the surface is curved, it is necessary to correct the crack length for the curvature of the surface. This is done by first measuring x_{off} and x_{crack} relative the center line and then calculating ϕ_{off} and ϕ_{crack} according to equation 3.4:

$$\phi_{\text{off/crack}} = \arcsin\left(\frac{x_{\text{off/crack}}}{r}\right) \tag{3.4}$$

Thereafter, the true crack length, defined as the crack length on the mantle surface, in the horizontal direction, can be determined by equation 3.5:

$$\text{Crack length}_{\text{true}} = (\phi_{\text{crack}} - \phi_{\text{off}}) \cdot r \tag{3.5}$$

3.4.4 Paper D - In situ uniaxial fatigue crack propagation

In this study, in-situ uniaxial fatigue crack propagation experiments were conducted, using predeformed single edge notch tension (SENT) specimens made from pearlitic rail steel R260, see Figure 3.13.

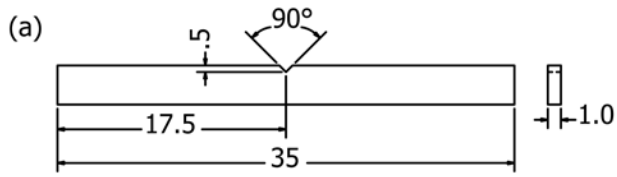

Figure 3.13: Geometry and dimension of the SENT specimen used in **Paper D**

The aim of this study was to investigate the influence of large shear deformation (anisotropy) on the crack growth behavior in terms of crack propagation and crack path. For this purpose, solid cylindrical test bars were predeformed by twisting 6x90° (PD6) according to the predeformation method described in section 3.1. The sent specimens were then extracted from the predeformed test bars by using spark erosion machining. To investigate the influence of anisotropy on crack propagation behavior, SENT specimens were extracted both tangentially and radially from the predeformed cylindrical test bars, orienting the notches differently relative to the microstructure alignment. In addition, undeformed SENT specimens were naturally included as reference.

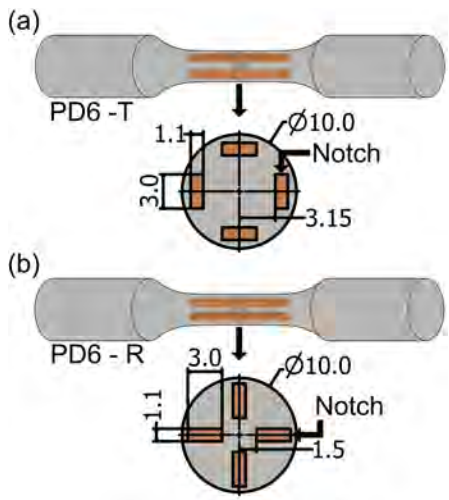

Figure 3.14: Illustration of SENT specimen extraction from predeformed test bars in **Paper D**. (a) shows the PD6 - T specimen and (b) shows the PD6 - R specimen.

The distribution of shear strain following predeformation may be considered to be radially linear according to the simple shear model. Consequently, the shear strain gradient in the extracted SENT specimens can be calculated by determining the surface shear strain after predeformation, as done in **Paper A**. In Figures 3.15a and 3.15b, the shear strain gradient as a function of distance for the notch is plotted at three different thicknesses for PD6-T respectively PD6-R. The tangentially extracted specimens exhibit a nearly constant level of shear strain along the notch for each material layer. However, a strain gradient is evident across the thickness. In contrast, the specimens extracted radially exhibit a pronounced strain gradient along the notch, whereas the strain gradient across the thickness is sufficiently small to be neglected.

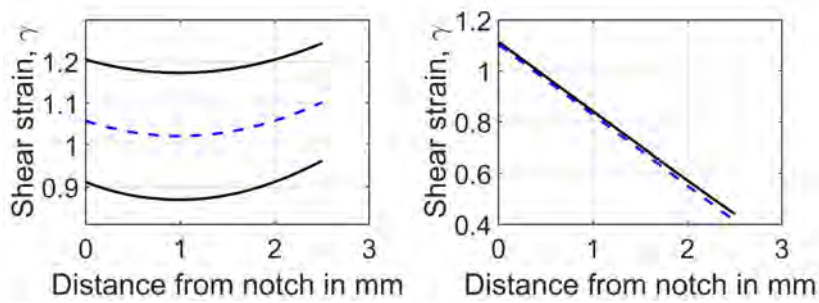

Figure 3.15: Shear strain distribution of (a) PD6-T (b) PD6-R single etched notched specimens.

In addition to the differences in strain gradient between the two SENT specimens, the notch is oriented differently with respect to the microstructure alignment. The microstructure alignment in the tangential direction after predeformation to PD6 is shown in the micrograph in Figure 3.16a. A visualization of the notch orientation relative the microstructure alignment can illustrated as in Figure 3.16b. Noting that orientation of the cementite lamellae has a statistically preferred direction but it is a distribution so it cannot be considered as globally aligned as explained and shown in [16].

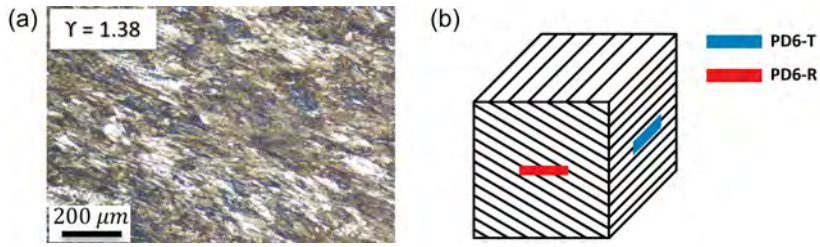

Figure 3.16: The microstructure alignment of PD6 test bars close to the surface along the tangential direction is shown i (a). In (b) the notch location of the PD6 single edge notched specimens are illustrated with respect to microstructure alignment. Note, the inclined lines represents shear deformation and not orientation of cementite lamellae.

The fatigue crack propagation experiments were load controlled with a triangular load waveform. To avoid buckling, the load ratio was set to R = 0.1. The maximum load was set to 125% of the offset yield strength in tension for undeformed material which corresponds to 667.75 MPa. The magnitude of the maximum load was experimentally determined to give a short fatigue life as in-situ fatigue testing is very time consuming. The displacement rate was set to 8 μ/s (corresponding to approx 0.03 Hz) to avoid heating of the tensile stage. Figure 3.17 shows the tensile-compression stage used in this study along with a mounted sent specimen. The sent specimens were mirror polished prior testing and either etched or prepared with a speckle pattern for DIC measurement using FIB.

Figure 3.17: In-situ tensile stage with mounted SENT specimen.

Prior testing, a large area map around the notch were acquired and was used as a reference to see the surface changes imposed by the load. During testing, the scanning speed to obtain high resolution images are much lower than the displacement rate of the test bar. Accordingly, the test must be paused to obtain the high quality micrographs required for monitoring crack growth and surface damage such as strain localization and debounding at manganese sulfides (MnS). The test were interrupted regularly, in intervals of maximum 20 cycles. During each interruption a panorama image was acquired around the notch and high magnification micrographs of the crack(s) and other regions of interests were acquired.

3.4.5 Paper E - Four point bending

In **Paper E**, an in-field railhead crack detection method based on digital image correlation (DIC) measurements was proposed. This method utilizes the bending moments induced by the train, and by comparing the same area in both the loaded and unloaded states, it is possible to use DIC to measure the surface strain field, where strain concentrations are expected at surface-breaking cracks. To simulate rail bending and evaluate the proposed method, a fixture for four-point bending was built. Two rail sections were connected by threaded rods, as shown in Figure 3.18. To achieve four-point bending, and thereby a constant bending moment for the region of interest, two hydraulic cylinders were placed 210 mm from each rod. The pressure was monitored by an electronic pressure sensor and controlled using a manual pump.

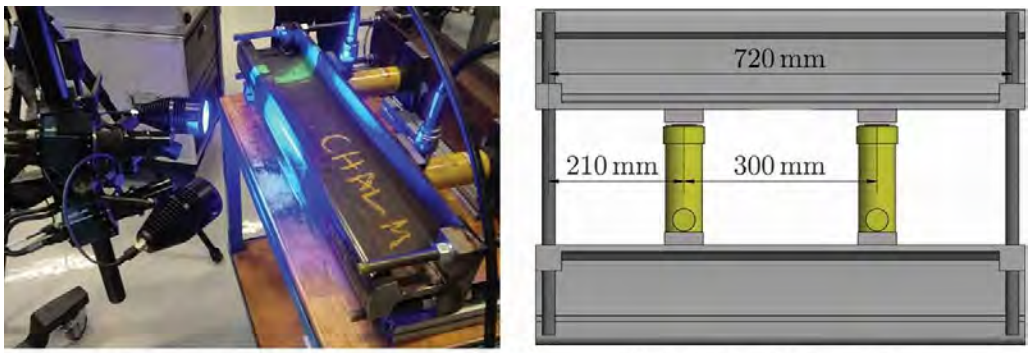

(a) Picture of DIC experiment (b) Schematic of bending fixture

Figure 3.18: Experimental setup for DIC measurement of 4-point bending in **Paper E** [43]

The commercial GOM stereo-DIC system was used in this study for the DIC measurements. Prior to testing, the rail surface was prepared with a speckle pattern: a white background with black speckles covering approximately 50% of the rail surface. The surface strain was then measured for the unloaded reference state and for two bending moments corresponding to 7.5 kNm and 15 kNm. To increase the coverage of the DIC measurements, images acquired from eight different camera positions were stitched together.

Chapter 4

Summary of results

4.1 Paper A - Uniaxial fatigue crack propagation

This section presents the main results of **Paper A** "Fatigue Crack Propagation on Uniaxial Loading of Biaxially Predeformed Pearlitic Rail Steel". The reader is referred to the attached paper for a detailed description and analysis of the results.

4.1.1 Hardness and shear strain measurement

In **Paper A**, the predeformed test bars were characterized in terms of hardness distribution and surface shear strain. The hardness distribution along the radial direction is shown in Figure 4.1.

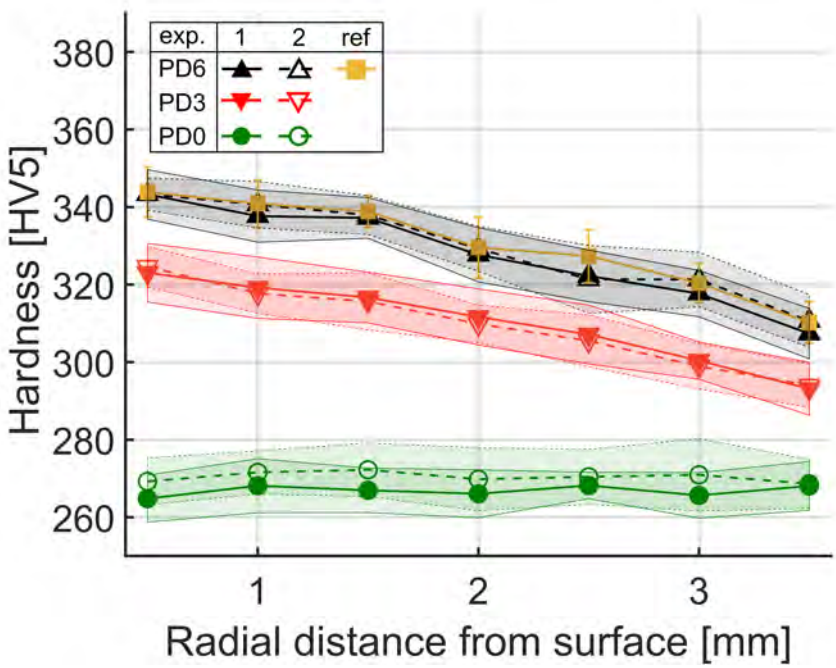

Figure 4.1: Hardness measurement of undeformed and predeformed test bars.

A total of 112 indents were made for each test bar, with an even distribution across the different radial positions. This equates to 14 indents around the specimen per radial position. The undeformed material exhibits a uniform hardness distribution with an average value of 269 HV5 and standard deviation of 7 HV5, which is in accordance with the material specification of the R260 steel, see EN 16674-4 [44]. Conversely, predeformation induces an almost linear gradient in hardness for both the deformed material states. The hardness values are approximately 20 HV5 units higher in PD6 when compared to PD3. In addition, there is good agreement in the hardness values observed between similar levels of shear strain, with parallel curves observed between PD3 and PD6. For instance, the hardness level at a depth of 2.5 mm in PD6 is comparable to that at a depth of 0.5 mm in PD3 (given that for half the radius, half of the surface shear strain is expected). Finally, the reference sample aligns with the hardness curves of PD6, showing that plastic deformation was initially concentrated in a region near the notch and subsequently concentrated at the crack front following propagation of the crack through the notch.

From the principles of solid mechanics, the hardness distribution can be explained by the stress and strain distribution. An estimation of the shear strain distribution can be derived on the basis of the assumption that, during torsion, each cross-sectional plane will remain planar. Under this assumption, the shear strain is found to decrease in a linear manner towards the centre, which could explain the observed macroscopic linear hardness gradient. It is important to note that strain localisation occurs, for example, in slip bands along the interface between cementite and ferrite. Consequently, local differences will exist. While the assumption of planar cross-sectional planes during torsion provides a reasonable estimation for the shear strain distribution, the stress distribution during predeformation remains unknown. This is primarily due to plastic deformation, which results in an increase in diameter accompanied by a subsequent decrease in axial compressive stress.

Nikas et al. [31], measured the interlamellar spacing and dislocation density after predeformation. The dislocation density was found to increase almost linearly with increasing shear strain, while only a slight decrease in interlamellar spacing was observed. It is well known that the yield strength of pearlitic steels follows a Hall-Petch relationship with respect to interlamellar spacing, with the primary factor governing the yield strength being the interlamellar spacing. However, the decrease in interlamellar spacing was observed to be very small and thus it cannot explain the increase in hardness. By accounting for the increased dislocation density, Nikas et al [31] found good agreement with the increase in hardness.

The surface shear strain was measured by using a laser etched grid (see section 3.1) and the results are presented in Table 4.1. Two columns are shown, the shear strain after predeformation and the shear strain after reprofiling (calculated by assuming linear shear strain distribution). The standard deviation is low, and by also considering the hardness measurements, the predeformation method can be considered to have good repeatability.

Table 4.1: Shear strain measurement

	PD3	PD6
Average surface shear strain after pre-deformation	0.74 ± 0.05	1.52 ± 0.05
Average surface shear strain after reprofiling	0.66 ± 0.05	1.38 ± 0.05

4.1.2 Crack measurement and crack path

The surface crack length measurements for the nominal stress amplitudes corresponding to 60 % and 70% of the offset yield strength of virgin rail material are presented in Figures 4.2 and 4.3. For each test bar, two cracks were measured, one on either side of the notch. The crack propagation rate is observed to be initially constant, and as the crack becomes longer, a transition to exponential crack growth occurs. The transition to exponential crack growth is expected and can be explained by the succesive load increase at the crack front. The load increase is a function of area reduction which can be assumed to exponentially increase as the crack propagates through the notch (based on the semi-elliptical fracture surface). Initially, the area reduction can be considered to be negligible and the stress concentration induced by the notch dominate the local stress condition. Interestingly, in each experiment, the crack propagation rate of the two cracks extending from the sides of the notch is similar, indicating that crack growth becomes symmetric around the notch. The two cracks then joins to form a semi-elliptical crack front.

A significant difference in crack propagation resistance is observed when comparing undeformed and predeformed material. For both stress amplitudes, the fatigue crack propagation resistance was highest in the predeformed material. At the lower stress amplitude, the predeformed material exhibited a significantly higher fatigue crack propagation resistance than the undeformed material, with the predeformed material enduring almost twice the number of cycles for the same surface crack length. In the case of the higher stress amplitude, the difference in crack propagation resistance between the undeformed and predeformed material is even more pronounced. When comparing the predeformed material states, it was observed that the crack propagation resistance was comparable, with one exception for test bar 1 of PD3, which endured approximately 25% more cycles.

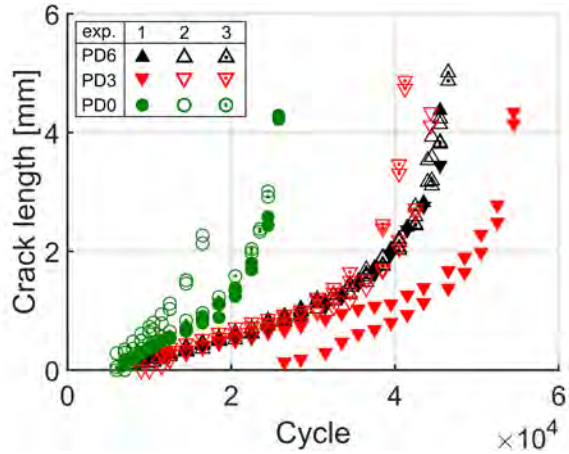

Figure 4.2: Crack propagation measurement from test bars subjected to a load amplitude of 60 % of the offset yield strength.

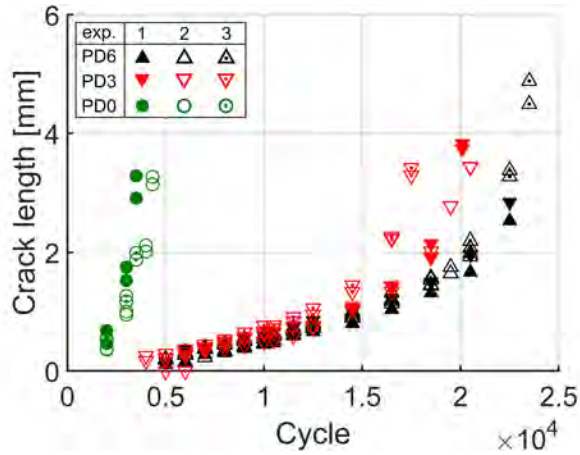

Figure 4.3: Crack propagation measurement from test bars subjected to a load amplitude of 70 % of the offset yield strength.

The surface crack path was visualized by extracting the crack contour of the last measured crack before failure. This was done to examine if differences in crack path could be observed between the different material states. The crack contours are presented in Figures 4.4 and 4.5 for the respective stress amplitude. The overlayed grid in the figures represents the surface shear deformation resulting from twisting 6x90° (PD6), in the direction towards the microstructure. It can be observed that the crack growth direction for the undeformed and PD3 material state is on average straight with local crack kinking. The crack paths of the PD6 material state exhibit a comparable trend for the higher stress amplitude, with the crack growth occurring at a shallow angle for the lower stress amplitude. These findings indicate that the crack path is influenced by both the direction of the deformed microstructure and the magnitude of the applied axial load (magnitude of plastic deformation).

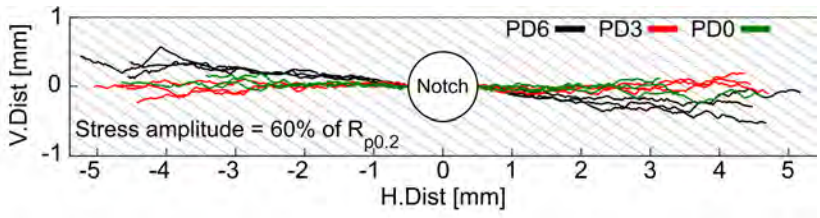

Figure 4.4: Digitized cracks for all test bars subjected to a nominal stress amplitude of 60% of the offset yield strength $Rp_{0.2}$.

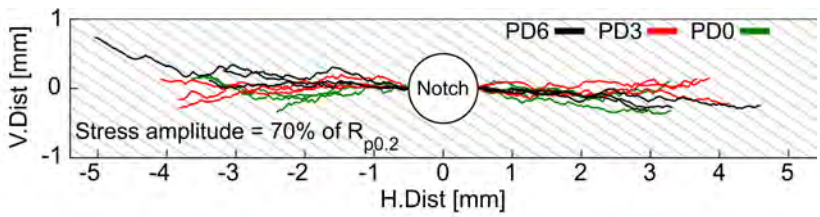

Figure 4.5: Digitized cracks for all test bars subjected to a nominal stress amplitude of 70% of the offset yield strength $Rp_{0.2}$.

The surface crack path was also examined using a scanning electron microscope (FEGSEM). A limited correlation was found between the orientation of cementite lamellae and the direction of the surface crack path. The variation of crack growth direction with respect to the orientation of the cementite lamellae is exemplified Figures 4.6 and 4.7. These micrographs qualitatively demonstrate that the surface crack growth direction varies. It can be observed that the crack only propagates along the cementite lamellae in small sections; see the detailed views B and A in Figures 4.6 and 4.7. In other sections, however, the crack propagates across the cementite lamellae, as exemplified by the detailed views A and B of Figures 4.6 and 4.7.

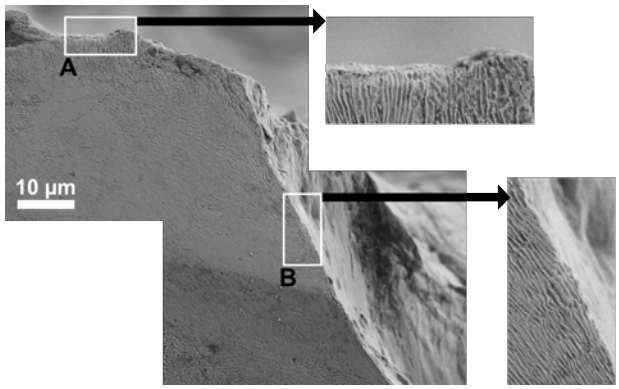

Figure 4.6: The surface crack path (on the lateral surface) for a PD3 test bar. The figure illustrates the observed variation in crack growth direction on the surface. Detailed views A and B illustrate the surface crack growth across and along the cementite lamellae, respectively.[43]

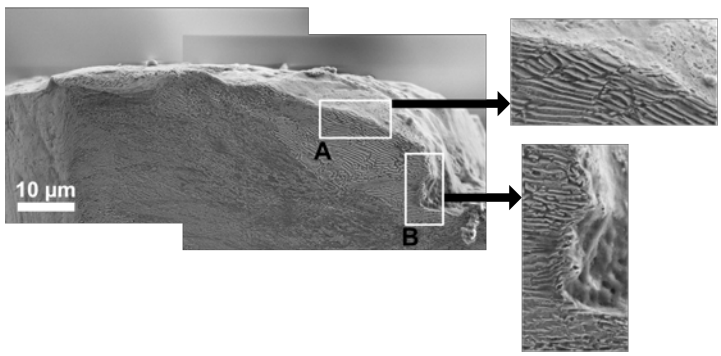

Figure 4.7: The surface crack path (on the lateral surface) for a PD6 test bar. The figure illustrates the observed variation in crack growth direction on the surface. Detailed views A and B illustrate the surface crack growth along and across the cementite lamellae, respectively. [43]

4.2 Paper B - Torsional fatigue crack propagation

4.2.1 Fatigue life and crack path

Axial and torsional stiffness was measured during the torsional fatigue experiments and was used as a comparative measure of the material damage evolution. The stiffness measurements were filtered with a modified running average (see **Paper B** for details) to reduce the scatter, primarily for the axial stiffness measurements. The filtered stiffness measurements for axial and torsional stiffness are presented in Figures 4.8 and 4.9, respectively. It can be observed that the scatter in the axial stiffness measurements are large, as shown by the standard deviation (wrt. the difference between filtered and unfiltered data). The scatter for the torsional stiffness measurement is very small, barely visible and this is because the torsional strain amplitude during the stiffness measurements were higher than the axial strain amplitude. The variation between each repeated test is observed to be lower than the difference between the different tests series. Thus, the axial stiffness measurements were considered as sufficiently reliable.

The fatigue life, which was defined as a 5% drop in axial stiffness was observed to be dependent on the material state, axial compressive load and direction of the torsional load. The fatigue life was longer for predeformed material and increased when a compressive axial load was applied. The compressive load influences the fatigue life more than the material, and the effect was similar for both material states. Reversing the direction of the torsional load increased the fatigue life of the material the most. These results were unexpected as more cracks grows along the direction of the deformed microstructure than in loading along the direction of the deformed microstructure.

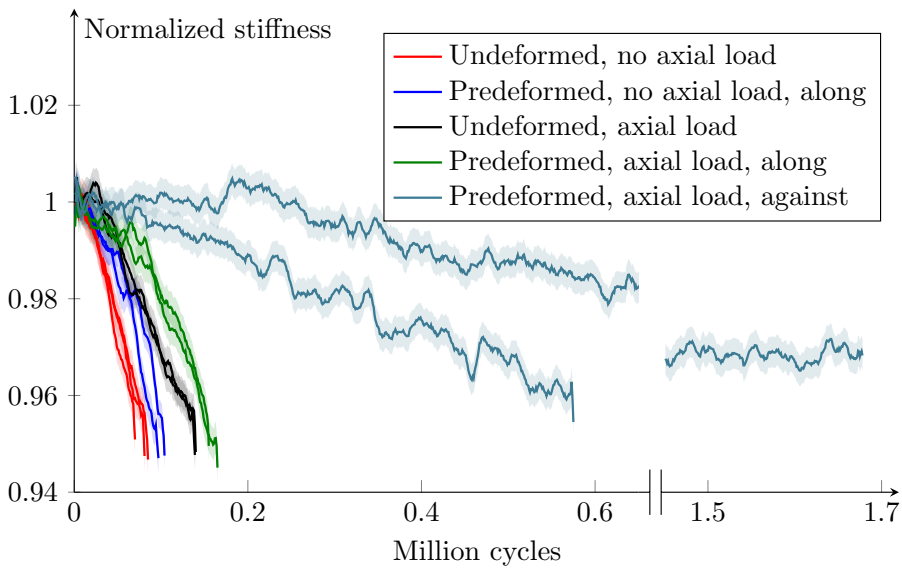

Figure 4.8: Axial stiffness evolution for different material and loading conditions. The shaded areas show ± one standard deviation.

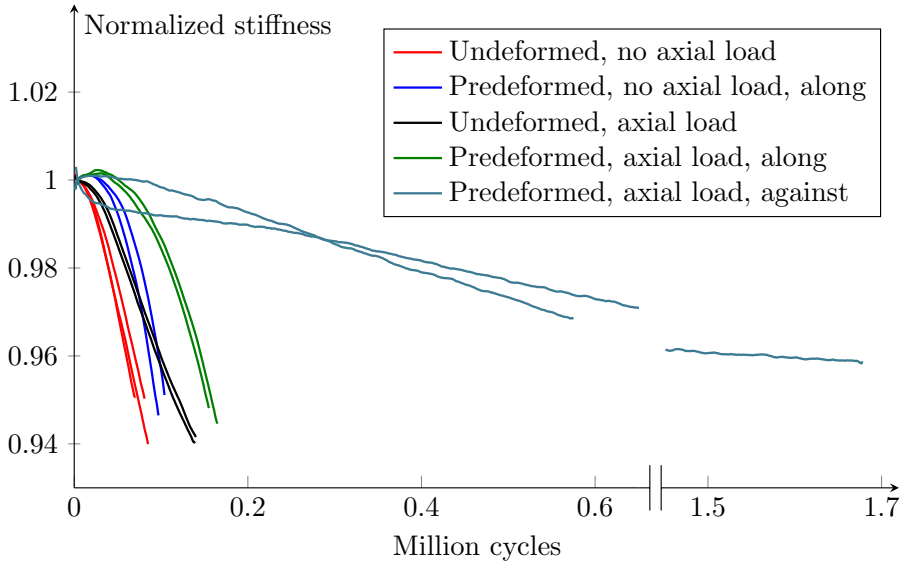

Figure 4.9: Torsional stiffness evolution for different material and loading conditions.

The fracture surfaces of all test bars were investigated. The crack paths and the shape of the fracture surfaces were found to be dependent on the material state and loading condition. It was observed that the fatigue zone in all experiments represents the growth of multiple cracks initiated along the circumference of the notch. Additionally, the fatigue zone can be characterized as a complex crack network; crack growth planes vary around the notch, and multiple cracks can be observed beneath the observed fracture surface. Notably, crack growth was predominantly inclined clockwise or counterclockwise for torsional loads applied along and against the direction of predeformation, respectively.

The fraction of cracks growing in the predominant direction was estimated by calculating the number and direction of cracks extending outside the notch. These measurements are listed in Table 4.2. The direction of inclined crack growth showed good agreement with the direction of remote principal stress, as derived from the torque response. For instance, the torque ratio $R_{Torque} = \frac{T_{min}}{T_{max}}$ for predeformed material loaded along the direction of predeformation was found to be close to zero. Consequently, the cyclic torsional load is close to pulsating, resulting in the majority of cracks growing in the clockwise direction. Conversely, the undeformed material exhibited a higher torque ratio, making the cyclic torsional load more alternating. In this case, the majority of cracks observed to grow in a clockwise direction were smaller. For further details, please refer to section 4.1 in **Paper B**.

Material state	Axial load	Torsional load direction	Fraction of cracks
PD0	0 MPa	Along	67% CW
PD0	-100 MPa	Along	68% CW
PD3	0 MPa	Along	86% CW
PD3	-100 MPa	Along	87% CW
PD3	-100 MPa	Against	63% CCW

Table 4.2: Fraction of cracks counted in the predominant direction on the fracture surface. CW - Clockwise and CCW - Counter clockwise direction.

The fracture surfaces of the undeformed specimens, with and without a superimposed load, appeared to be similar. A representative fracture surface for the undeformed material is presented in Figure 4.10. The fatigue zone is predominantly continuous and extends into the bulk with a relatively uniform depth. However, regions are observed where there are no apparent fatigue cracks, as shown in more detail in Figure 4.10c. Characteristic of these fracture surfaces is the factory roof-shaped fracture surface, resulting primarily from mode I crack growth. As described in the previous section, the crack growth direction is primarily inclined clockwise, as seen by the asymmetrical factory roof, with the longer side along the clockwise direction. The fracture surface of predeformed samples loaded against the direction of predeformation appears very similar to the undeformed samples, with two distinct differences: cracks are predominantly inclined counterclockwise, and the fatigue zone is not as uniform along the radial direction.

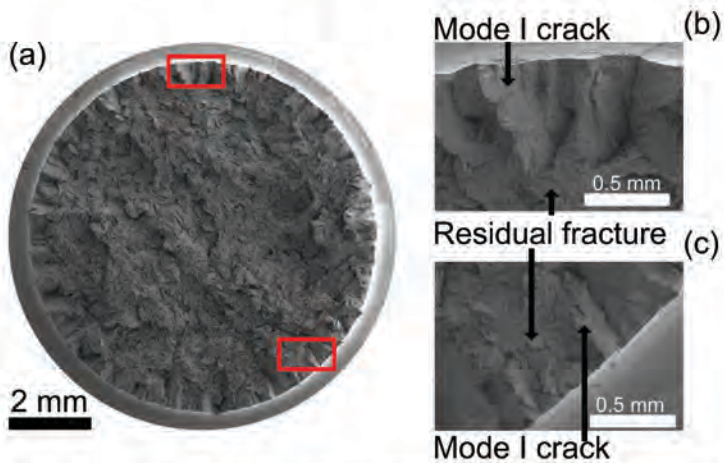

Figure 4.10: Representative fracture surface of undeformed test bars with shear load along the direction of predeformation.

The fracture surfaces of predeformed specimens, subjected to torsional loading along the direction of predeformation, are significantly different from those of the undeformed material state. In Figure 4.11, a representative fracture surface for predeformed specimens subjected to a compressive load during testing is shown. Characteristic of the fracture surfaces of the predeformed specimens, with or without a compressive axial load during testing, is the heterogeneous fatigue zone. The factory roof-shaped surface seen in the undeformed specimens is not evident. Instead, the fracture surface is characterized by inclined crack growth in the clockwise direction. It was observed that superimposing an axial compressive load changes the crack growth behavior. With a superimposed axial load, a tendency for deeper cracks was found, and crack growth was confined to fewer regions around the notch.

The topography of the fracture surface does not capture the complete crack growth behavior as many cracks are concealed. The crack network was therefore examined in more detail by transverse sectioning at different depths, as shown in Figure 4.11c. The transverse lines a-c correspond to the micrographs labeled a-c in Figure 4.12. These micrographs reveal crack growth beneath what is observed as residual fracture on the topography. These cracks are observed to mainly propagate against the direction of predeformation.

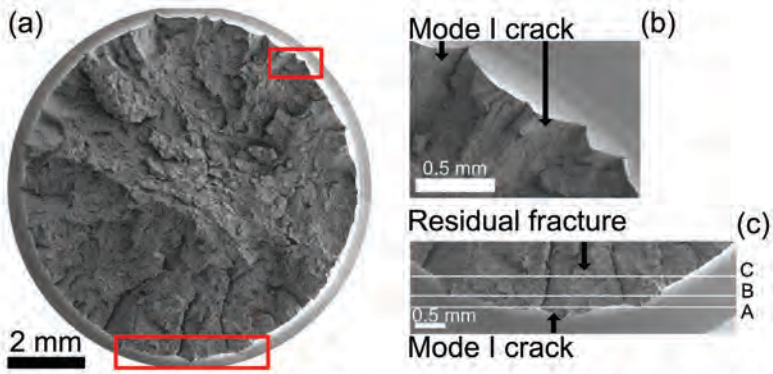

Figure 4.11: Representative fracture surface of predeformed test bars with axial load and shear load along direction of predeformation.

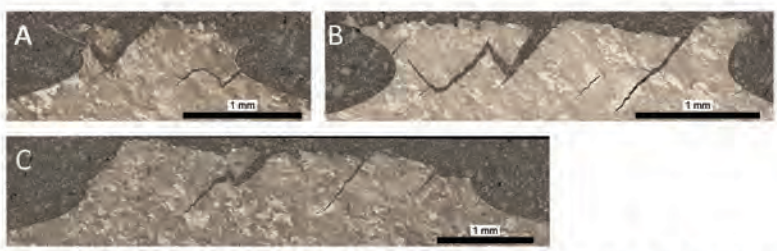

Figure 4.12: Radial view of crack network in a predeformed test bar at different depths from the notch root a) 51 μm b) 234 μm c) 547 μm.

4.3 Paper C - Multiaxial fatigue crack propagation

4.3.1 Hardness and mechanical response

The hardness distribution along the radial direction was measured after non-proportional multiaxial fatigue testing of smooth test bars. The hardness measurements are presented in Figure 4.13 and provide a comparative measurement of the effect of plastic deformation during fatigue loading in terms of flow stress. The predeformed specimens exhibit a linear hardness gradient. This hardness gradient was induced by predeformation, as quantified in **Paper A**, see section 4.1.1. The hardness of the predeformed specimens PD6 and PD3 after fatigue loading is found to be approximately 10 HV5 units lower than after predeformation. The hardness of the predeformed specimen PD1 has not been measured after predeformation, but it is expected that the hardness will be slightly lower after fatigue, as cyclic softening is observed for the axial load, as in the case of PD3 and PD6 specimens, see Figure 4.14. The multiaxial plastic straining can be considered to be confined to a rather thin surface layer as at larger depth the shear strain is not large enough to cause plastic deformation hardening.

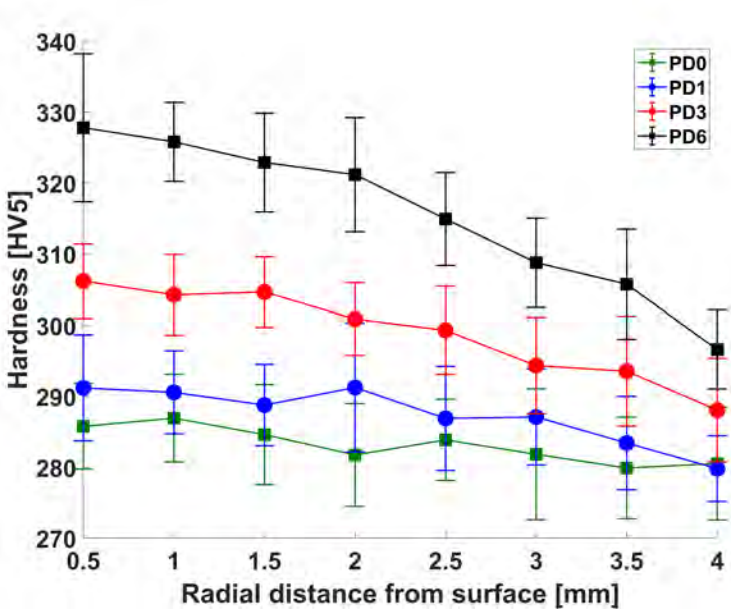

Figure 4.13: Hardness distribution as a function of radial distance after non-proportional fatigue loading of smooth test bars of different material states.

The evolution of the nominal axial stress amplitude and mean stress for notched and smooth test bars is shown in Figure 4.14. The difference between the notched and smooth test bars is small for the first 500 cycles. Beyond this point, the crack propagating from the notch is long enough to affect the structural integrity of the test bar, resulting in a drop in axial stress amplitude. The similar axial stress response indicates that the material in front of the crack, in the highly multi-axially strained region, strain hardens and compensates for the reduced load area. Axial and torsional stiffness measurements were made, but it was not possible to use these measurements as, for similar stiffness reduction, the surface crack length of the test bars was different. It was not possible to measure the crack depth, and therefore the stiffness measurements were considered too uncertain.

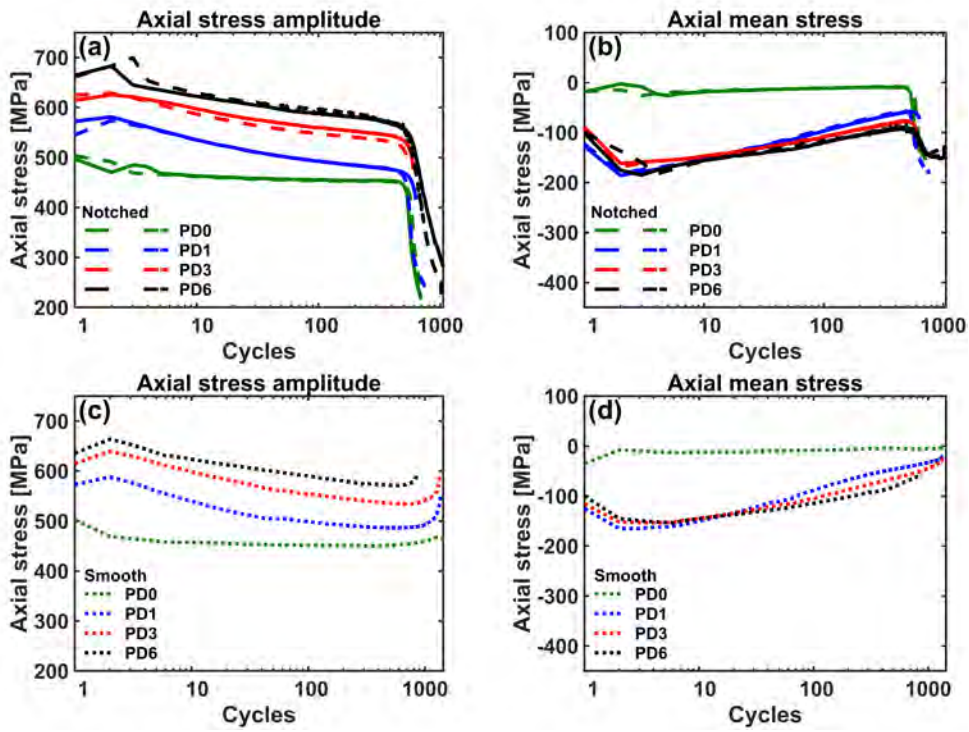

Figure 4.14: Comparison between the axial stress evolution of notched and smooth test bars at $\varepsilon_{eq} = 0.6\%$: (a) and (b) shows the axial stress amplitude and the axial mean stress with respect to the number of cycles for notched test bars. (c) and (d) show the axial stress amplitude and the axial mean stress with respect to the number of cycles for smooth test bars.

The evolution of torque response for notched and smooth test bars is shown in Figure 4.15. The torque response is presented in terms of torque amplitude and mean torque, as the shear stress cannot be determined without material modeling assumptions and finite

element analysis. Moreover, the torque response for the notched specimens is difficult to analyze: as the crack propagates, the torque response is influenced by crack face friction, which is affected by surface crack topography (and possible crack path) and wear that changes over time. The torque response of the notched and smooth test bars shows a difference in both torque amplitude and mean torque. For the notched specimens, the torque amplitude reduces slightly for the first 500 load cycles, followed by a subsequent drop as the crack becomes longer, i.e., the area of the fatigue zone becomes sufficiently large to affect the structural integrity of the test bars. One exception was observed for one PD6 specimen, for which the torque amplitude increased before dropping at 500 cycles. The difference in torque amplitude for the first 500 cycles could be due to measurement uncertainties, as the crack leading to fracture in the smooth specimens propagated through the extensometer indent, thereby possibly altering the relative angle between the extensometer pins.

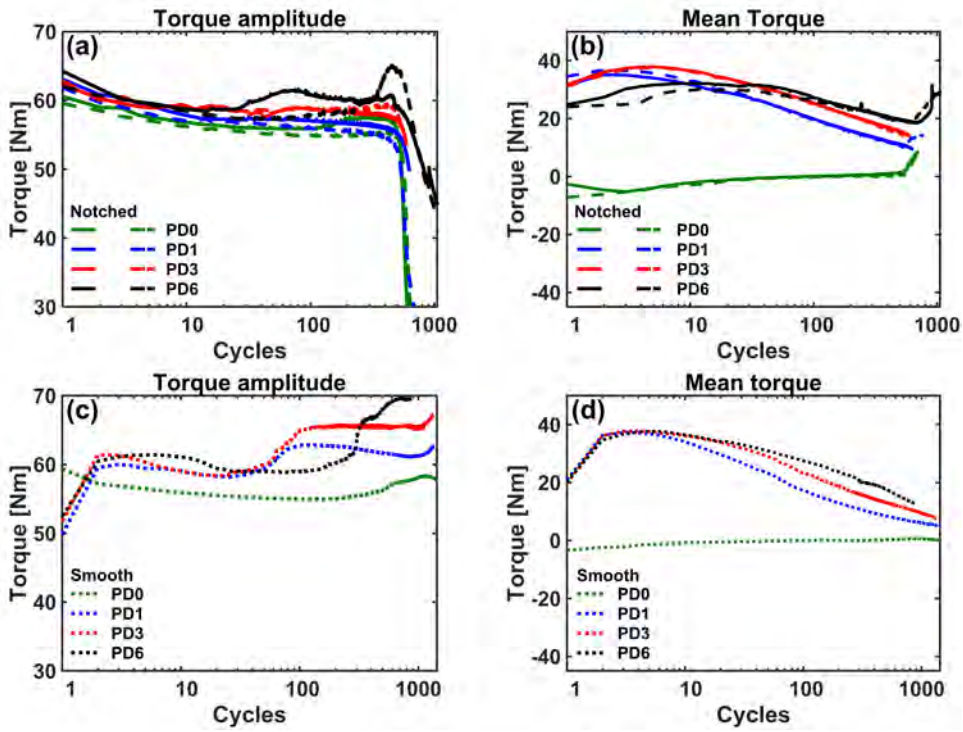

Figure 4.15: Comparison between the torque evolution of notched and smooth test bars for non-proportional loading at $\varepsilon_{eq} = 0.6\%$: (a) and (b) show the torque amplitude and the mean torque with respect to the number of cycles for notched test bars. (c) and (d) show the torque amplitude and the mean torque with respect to the number of cycles for smooth test bars.

4.3.2 Crack propagation and crack path

The notch was designed to initiate the crack at the pointy end on the left hand side, see Figure 3.8 in section 3.4.3. Cracks were always observed to first initiate on the left side, followed by subsequent propagation towards and away from the notch. A crack on the right side initiated after the left crack had propagated. The cracks on the left and right side of the notch merged into a single crack after reaching several millimeters in length, as measured from the surface.

The surface crack length for the cracks propagating away from the notch on the left and right side was measured. To make the surface crack propagation rates more comparable, the surface crack length were plotted against the number of measurements since a visible crack could first be detected. The surface surface crack length measurements are presented in Figures 4.16 and 4.18 for the surface crack on the left respectively right side of the notch. Interestingly, the crack propagation rate for the undeformed and predeformed material state is very similar. However, due to the variation between the duplicate tests it is not possible to determine if a significant difference in crack propagation rate is present. In the insert of Figure 4.16, the early crack growth is presented. For the cracks lengths presented, the crack growth is confined within a regions close to the mantle surface, where predeformation is the highest. Interestingly, the crack propagation rate is very similar, for details see **Paper C**.

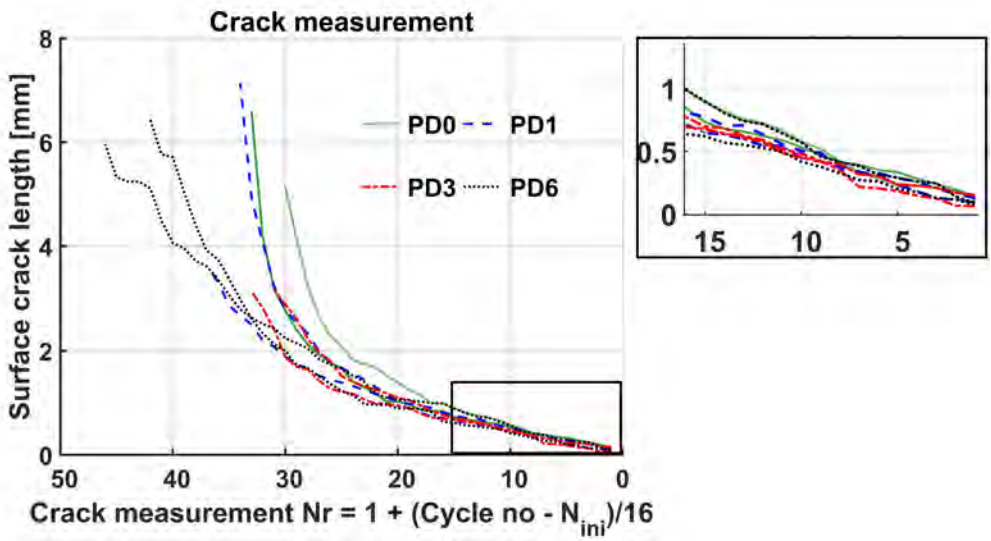

Figure 4.16: Figure showing the left crack length with respect to the crack measurement number. The insert shows the early surface crack propagation. The first crack measurement was made once a crack could be detected.

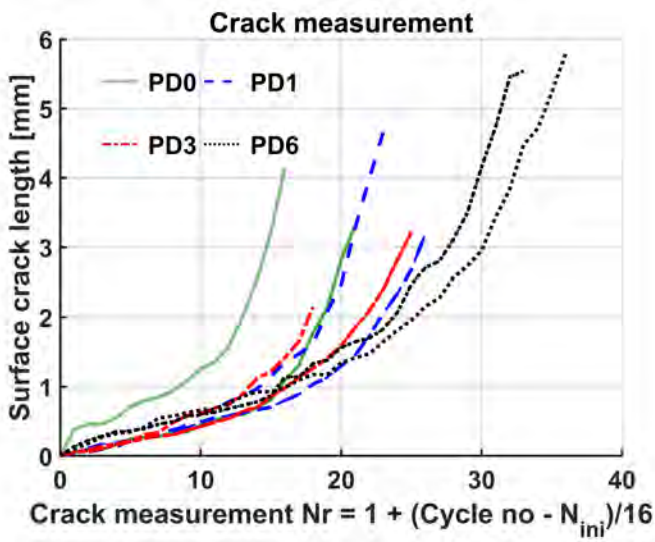

Figure 4.17: Figure showing the left crack length with respect to the crack measurement number. The first crack measurement was made once a crack could be detected.

The crack paths for the different material states are shown in Figure 4.18. It is evident that predeformation has a significant effect on the crack path. The difference between the undeformed material PD0 and PD1 is small. Both show an inclined crack growth, but the crack propagates at a slightly shallower angle for PD1. However, as the degree of predeformation increases to PD3, a marked difference is observed. The crack propagates transversely to the direction of the microstructure alignment resulting from the predeformation. In addition, the final crack length prior to fracture is much shorter as compared to the other material states. In the case of the material state PD6, the crack path is almost the mirror image of that of PD0, but with an even steeper inclination angle, clearly showing an effect of predeformation with the crack growing more towards the direction of microstructure alignment.

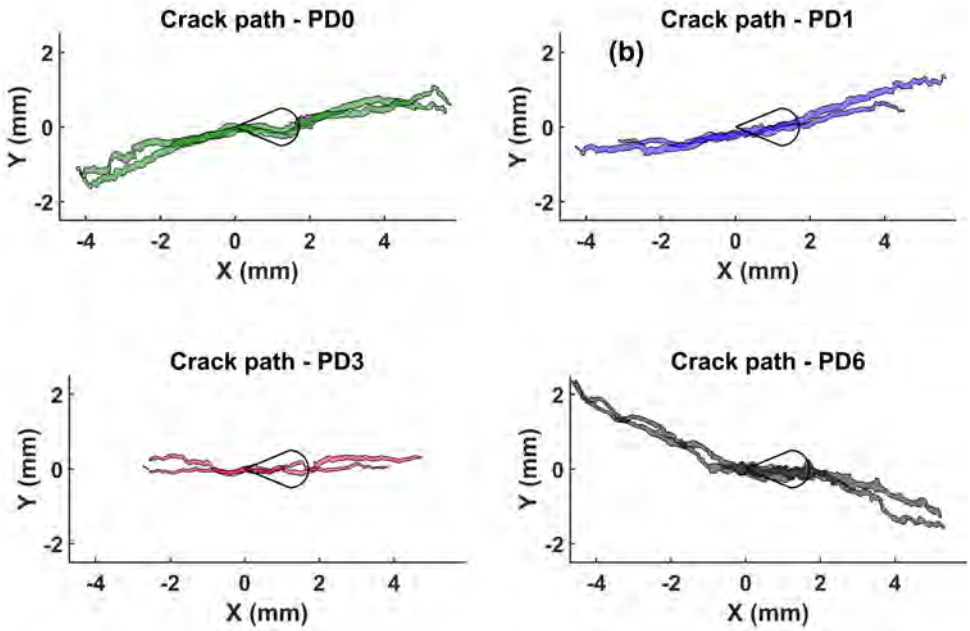

Figure 4.18: Crack path for (a) PD0, (b) PD1, (c) PD3 and (d) PD6. The crack path is a 2D projection of the surface crack. The origin is set at the left side of the notch as the crack first initiates there. Note that x is the projected distance from the origin.

4.4 Paper D - In-situ fatigue crack propagation

4.4.1 Crack growth

The crack length measurements were conducted on the etched side of the notch. The results are presented in Figure 4.19. It can be observed that for the undeformed material the crack propagation rate in the two duplicate test bars was similar. Comparing these results with the predeformed material states it is found that crack propagation resistance is higher in the latter. The number of cycles for failure is longer for PD6-T than PD6-R. Moreover, the crack propagation rate seems higher for the PD6-T specimens than PD6-R. The outlier is the second crack for PD6-R1 which initiated early but remained dormant after 100 cycles. The crack measurement results presented can however not be seen as representative for the crack propagation rate as only one side of the crack was possible to observe. From the fracture surface it is difficult to judge if the crack was propagating close to the surface or along the notch front, see Appendix for fracture surface micrographs.

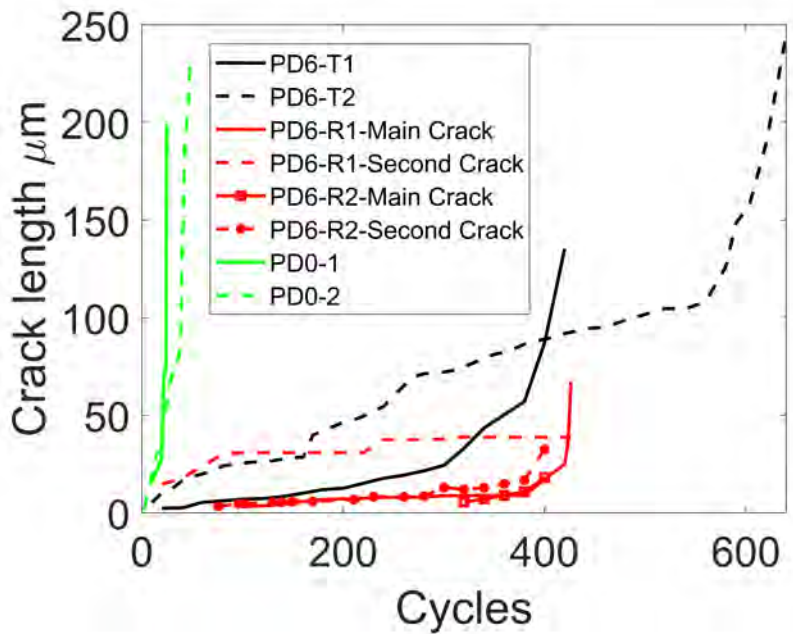

Figure 4.19: Surface crack length measurement

4.4.2 Crack path

The crack path of the last measured crack is presented in Figure 4.20. Since the top surface of each test bar was polished prior to testing, any surface topography is due to plastic deformation. Figure a shows the PD6-T crack appearance, with a relatively straight crack path initiated centrally in the notch area. Smaller cracks at manganese

sulphides are visible around the crack tip in figure b. The surface topography is not very strong in this material state. Figures d and e show the wide open main crack in the PD6-R pre-deformed material. The surfaces appear to have larger topography and indicate a likely multiple-site crack initiation, ahead of the main crack. However, further study is required to confirm this, as the three-dimensional crack growth could not be captured by this technique. Complementary tests using X-ray tomography would be more descriptive of the in-depth crack evolution. The secondary crack in figure c shows less plastic deformation and crack opening. The undeformed material in figures f and g, appears more similar to the PD6-R material with a large local plastic deformation and a rather short and open crack. The reason why the PD6-T specimens retain a flatter top surface could be due to the higher level of pre-deformation in this surface, with the material becoming progressively softer inwards.

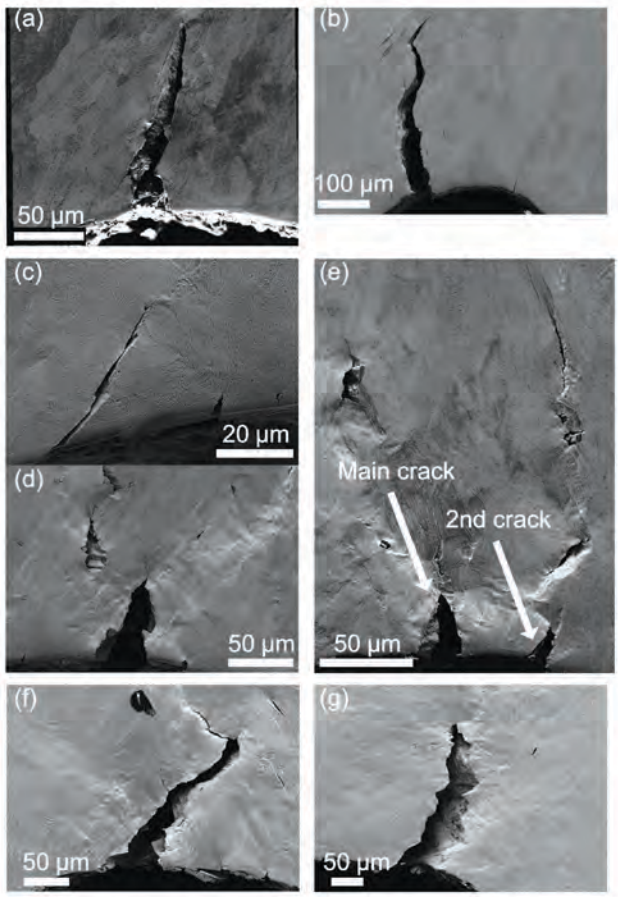

Figure 4.20: Crack length at last measured cycle: (a) PD6T-1 (b) PD6T-2 (c) PD6R-1 second crack (d) PD6R-1 main crack (e) PD6R-2 (f) PD0-1 (g) PD0-2

4.5 Paper E - Method for in-field railhead crack detection

This section presents the main results of **Paper E** "A method for in-field railhead crack detection using digital image correlation". The reader is referred to the attached paper for a detailed description and analysis of the results.

4.5.1 Digital image correlation and crack path

In **Paper E**, a new method for in-field railhead crack detection was proposed and evaluated under laboratory conditions. The method involves utilizing the bending moments caused by a rolling train. The bending moments along the train vary, and by considering a standard configuration of a freight train with a 25-ton axle load, it can be found that the bending moment for a section between the two bogie pairs is a convex function with a minimum value close to 0 kNm (see Figure 4.21). When the bending moment is positive, the tensile strains open the surface cracks, causing a displacement jump over the crack mouth that is sufficiently small to be detected by DIC as a strain concentration. For this purpose, two cameras are considered: Camera A, which takes a reference image at close to zero bending moment, and Camera B, which acquires an image of the same area as the reference image from Camera A as the train moves.

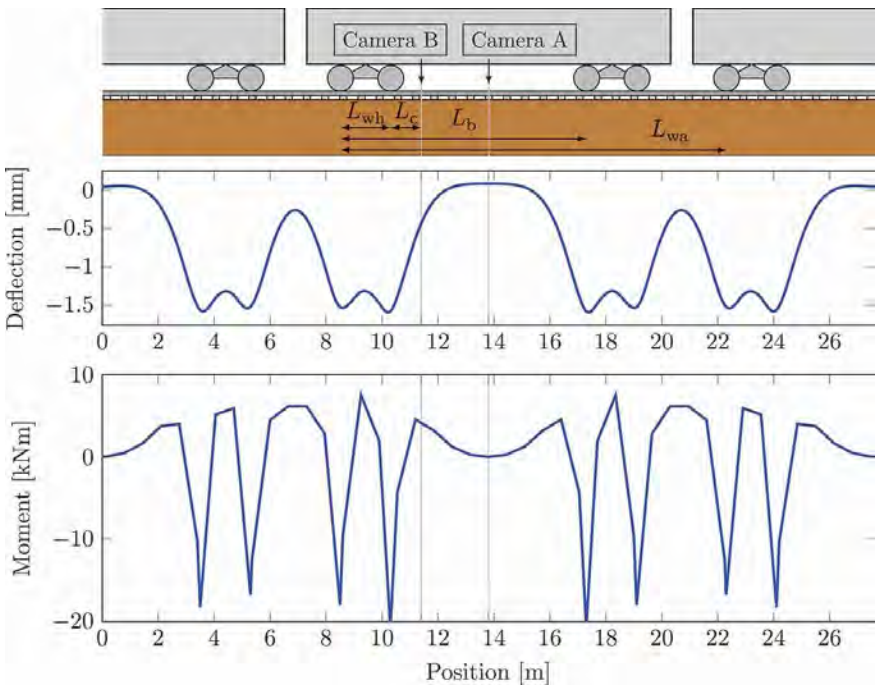

Figure 4.21: Rail deflection and bending moment due to a train passage [43].

To simulate rail bending in laboratory conditions, a 720 mm long rail section from the Swedish mainline was subjected to four point bending at two different loads, corresponding to 7.5 kNm and 15 kNm. The results from the DIC measurements showed relatively low signal to noise ratio for a bending load of 7.5 kNm. From the bending moment prediction for a freight train in Figure 4.21 the maximum positive bending load was only 3.8 kNm. However, as discussed in Section 5.1 in **Paper E**, it is possible to safely increase this load to 10 kNm by optimizing train parameters.

The strain field resulting from a bending load of 15 kNm is presented in Figure 4.22. The location of the DIC measurements is shown in Figure 4.23. From the DIC measurements surface cracks were successfully identified by the strain concentrations seen as yellow bands. The white regions corresponds to locations of high surface irregularities and can thus not be identified by the DIC algorithm. In addition, artefacts are seen at reference marks B and F.

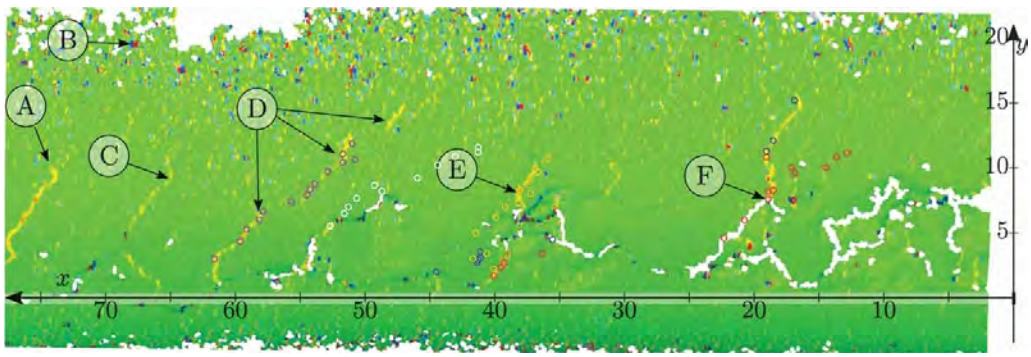

Figure 4.22: Strain field measured by DIC after subjecting the rail section to a bending moment of 15 kNm [43].

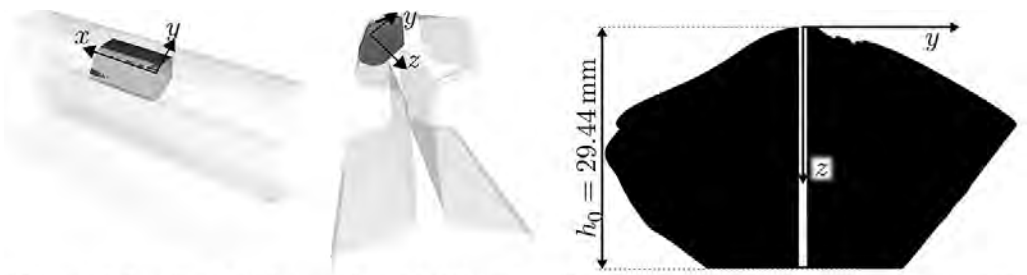

(a) Sample's location in a 3d-scanned model of the rail.

(b) Sample profile including reference mark (white line). The gauge corner is on the left side.

Figure 4.23: Rail sample used for DIC measurements and characterization of the crack network [43].

The performance of the proposed method was investigated by examining the crack network of the rail sample in detail through serial sectioning. The surface of the rail sample was ground in steps of approximately 0.25 mm along the z-direction according to Figure 4.23. To identify the cracks, the surface was semi-polished but not fully polished, as this makes image stitching difficult. By tracing the crack network through serial sectioning, it was possible to correlate surface-breaking cracks with the strain concentrations observed in Figure 4.22. This is exemplified in Figure 4.24 for z=-1.51 mm. However, the intricate crack network makes it very difficult to establish a clear correlation between the cracks and the surface strain measurements. Based on these findings, and supplemented by finite element analysis of cracks with different depths and inclination angles, it was hypothesized that the crack depth correlates with the surface strain concentrations as measured with DIC.

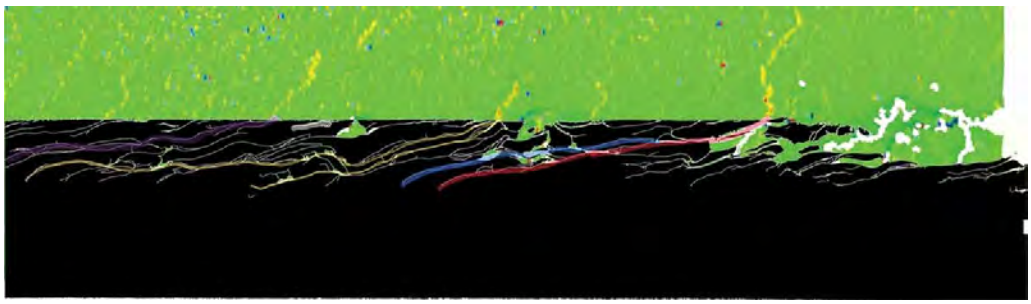

Figure 4.24: Correlation between cracks and DIC surface strains at z = -1:51 mm [43].

Chapter 5

Conclusions

In **Paper A** the effect of larger shear deformation on crack propagation was investigated. The crack propagation rates in undeformed and predeformed material was measured and the crack paths were investigated. The investigation lead to the following conclusions:¨

- Fatigue crack propagation resistance is significantly higher in predeformed material under stress controlled, constant amplitude fatigue loading.
- The degree of predeformation has limited effect on fatigue crack propagation resistance when comparing the predeformed states PD3 and PD6.
- The direction of surface crack growth in the predeformed states PD3 and PD6 does not follow the direction of the overall microstructure alignment.
- The crack paths in both undeformed and predeformed material was tortuous.

In **Paper B**, a new fatigue test method under loading conditions similar to rolling contact loading, accounting for the large accumulated shear strains close to the surface, was proposed. The method has been applied to investigate the influence of accumulated shear strains, compressive stresses, and loading direction in the R260 rail steel. The main findings are:

- The torque range is similar for all cases but the mean torque depends on predeformation and load direction.
- Compressive axial load prolongs the fatigue life while having negligible influence on the torque.
- The predeformed material sustains more cycles, even though loading along the predeformation direction increases the mean torque.
- Loading against the predeformation direction increases the fatigue life even though cracks grow in a weaker microstructural direction. This result was attributed to the lower mean torque.
- The crack growth direction correlates strongly with the mean torque.
- Complex crack networks, similar to those observed in rail field samples, form around the notch.

In **Paper C**, we have investigated the effect of large shear deformation on the fatigue characteristics of the pearlitic rail steel R260 subjected to strain controlled multiaxial fatigue loading. We considered undeformed material and three deformed material states corresponding to the material state at different depths from the highly deformed surface material found in used rail heads. The main findings are:

- The crack path is strongly influenced by the degree of predeformation. Increasing the predeformation causes the surface crack to propagate closer to parallel to the direction of microstructure alignment. For the material state predeformed to a surface shear strain of $\gamma = 1.38$, the crack propagated close to the direction of microstructure alignment, whereas for $\gamma = 0.7$ the crack path is almost horizontal which means the crack propagates at a larger angle to the microstructure alignment.

- The final crack surface crack length prior final fracture is much shorter for the material state predeformed to a surface shear strain of $\gamma = 0.7$ where the crack path is horizontal as compared to the other material states which shows an inclined crack path.

- The surface crack propagation rate is similar for all material states for the first millimeter of crack growth but because of the variation of surface crack propagation rate for longer cracks it is not possible to determine if there is a difference in crack propagation rate between the material states.

- The predeformed material states cyclically softens when subjected to non-proportional multiaxial fatigue loading in agreement to what is observed for uniaxial strain-controlled fatigue loading.

In **Paper D** we have characterised crack growth and crack paths in relation to the aligned microstructure in anisotropic pre-deformed pearlitic rail steel using small SENT specimens. Two orientations for the pre-deformed material were considered and undeformed material was used as reference. Cyclic loading was conducted in situ using a tensile stage in a scanning electron microscope. The applied tensile load was pulsating with a load ratio R = 0.1. The maximum nominal stress was set to 125% of the yield stress for the undeformed material. The surface crack growth was measured and the crack paths and fracture surfaces were examined. The main finding of this study are:

- The first load cycle strain hardens the material ahead of the notch for all test cases. Ratchetting occurred at a moderate level for predeformed material states and at a higher level for the undeformed material state. Despite ratchetting, the stiffness and hysteresis loop remain close to constant until the next last load cycle. Compliance measurements based on displacement are not sensitive enough when cracks are as small as in these experiments.

- The surface crack growth rate is higher in the undeformed material and it endures less cycles to failure than the predeformed material states. For the pre-deformed materials the critical crack length seem dependent on orientation of notch vs anisotropy.

- The energy absorption on fracture was the highest for undeformed material followed by the predeformed states.

In **Paper E**, a new method for in-field rail crack detection using digital image correlation was proposed. In the proposed method, two separated cameras are mounted on a measurement train. The load from the measurement train induces a surface strain field on the railhead surface that is measured using digital image correlation. The proposed method was evaluated under laboratory conditions and the method showed potential to improve rail condition monitoring. The main findings from this study are:

- Using digital image correlation it is possible to explicitly describe surface breaking cracks for bending moment within the safe limits of rail loading.
- Supplemented by finite element analysis of cracks with different inclination angles and depths, the proposed method is highly sensitive to crack depth.
- The strain field from the DIC measurement correlated with the 3-dimensional crack network created by serial sectioning.

Chapter 6

Future work

In this thesis work, the effect of large shear deformation on the fatigue crack behavior has been investigated. The contribution of this work can serve as a basis for future studies in the efforts made to understand the material behavior of the severely deformed surface layer and in the end mitigating the effects of rolling contact fatigue. The predeformation method used in this study to replicate the material state of surface layers is promising. The next logical step based on the conducted studies are:

- Large shear deformation cause work hardening, induces residual stresses and generates microstructure alignment. To fundamentally understand the effect of large shear deformation it is essential to isolate the effects of work hardening and microstructure alignment. Heat treatment for stress relief is suggested for which the critical step is to avoid spheroidization and changes in crystallographic orientation. To validate such heat treatment, it is crucial to conduct investigate the same area prior to and after heat treatment which could be achieved by conducting the heat treatments in an inert gas environment and crystallographic investigation.

- The multiaxial fatigue and crack propagation behavior of the severely deformed surface layer of deformed railheads is important to understand in the efforts made for improving maintenance guidelines and safety. To study the multiaxial fatigue behavior, axi-symmetric test bars with a similar material state as found in the top surface layer rail are required. The method used in this thesis work can achieve shear strains up to 2.3. However, much higher shear strains can be found in the very top surface layer of railheads. To achieve even higher shear strains by predeformation, a next step is to further develop this method by e.g., using test bar geometries that can withstand higher compressive loads without buckling.

- It is possible to extract specimens from predeformed test bars for in-situ fatigue crack propagation. In this thesis single edge notch tension specimens were extracted from predeformed test bars along different direction relative the microstructure alignment. However, crack initiation from the notch was not well defined. The next step is to introduce a pre-crack prior to fatigue testing as this gives a more well defined starting condition. To study the material state close to the surface of the predeformed test bars, the extracted specimens needs to be thin. Thus, the buckling resistance is very limited and the pre-crack needs to be introduced in tension. Consequently, the pre-crack should be introduced by first making a very sharp stress concentration, such as cutting a thin groove with diamond wire cutting.

References

[1] H. Ritchie, M. Roser, and P. Rosado. CO+ and Greenhouse Gas Emissions. *Our World in Data* (May 2020).

[2] R. Lewis and U. Olofsson. "Basic tribology of the wheel-rail contact". *Wheel-Rail Interface Handbook*. Elsevier Ltd, Sept. 2009, pp. 34–57.

[3] D. A. Porter, K. E. Easterling, and M. Y. Sherif. *Phase transformations in metals and alloys, third edition*. CRC Press, Jan. 2009, pp. 1–521.

[4] N. Guo and Q. Liu. Back-scattered electron imaging combined with EBSD technique for characterization of pearlitic steels. *Journal of Microscopy* **246**.3 (June 2012), 221–228.

[5] H. Bhadeshia and R. Honeycombe. "Iron-Carbon Equilibrium and Plain Carbon Steels". *Steels: Microstructure and Properties*. Elsevier, Jan. 2017, pp. 59–100.

[6] A. R. Marder and B. L. Bramfitt. The effect of morphology on the strength of pearlite. *Metallurgical Transactions A* **7**.2 (Feb. 1976), 365–372.

[7] N. E. Dowling. *Mechanical Behavior of Materials - Engineering Methods for Deformation, Fracture, and Fatigue*. Pearson Education, 2012, pp. 1–960.

[8] D. I. Fletcher, F. J. Franklin, and A. Kapoor. "Rail surface fatigue and wear". *Wheel-Rail Interface Handbook*. Elsevier Ltd, Sept. 2009, pp. 280–310.

[9] A. Ekberg and E. Kabo. "Fatigue of railway wheels and rails under rolling contact and thermal loading-an overview". *Wear*. Vol. 258. 7-8. Elsevier, Mar. 2005, pp. 1288–1300.

[10] S. Iwnicki, S. Björklund, and R. Enblom. "Wheel-rail contact mechanics". *Wheel-Rail Interface Handbook*. Elsevier Ltd, Sept. 2009, pp. 58–92.

[11] M. Schilke. *Thesis for the degree of doctor of philosophy - Degradation of Railway Rails from a Materials Point of View*. 2013.

[12] A. F. Bower and K. L. Johnson. Plastic flow and shakedown of the rail surface in repeated wheel-rail contact. *Wear* **144**.1-2 (Apr. 1991), 1–18.

[13] W. R. Tyfour, J. H. Beynon, and A. Kapoor. Deterioration of rolling contact fatigue life of pearlitic rail steel due to dry-wet rolling-sliding line contact. *Wear* **197**.1-2 (Sept. 1996), 255–265.

[14] A. Ekberg, B. Åkesson, and E. Kabo. Wheel/rail rolling contact fatigue - Probe, predict, prevent. *Wear* **314**.1-2 (June 2014), 2–12.

[15] *Rolling Contact Fatigue: A Comprehensive Review*. Tech. rep. 2011.

[16] K. A. Meyer, D. Nikas, and J. Ahlström. Microstructure and mechanical properties of the running band in a pearlitic rail steel: Comparison between biaxially deformed steel and field samples. *Wear* **396-397** (2018), 12–21.

[17] F. A. Alwahdi, A. Kapoor, and F. J. Franklin. Subsurface microstructural analysis and mechanical properties of pearlitic rail steels in service. *Wear* **302**.1-2 (Apr. 2013), 1453–1460.

[18] M. Sato, P. M. Anderson, and D. A. Rigney. Rolling-sliding behavior of rail steels. *Wear* **162-164**.PART A (Apr. 1993), 159–172.

[19] C. Kammerhofer et al. Influence of morphology and structural size on the fracture behavior of a nanostructured pearlitic steel. *Materials Science and Engineering A* **585** (Nov. 2013), 190–196.

[20] A. Hohenwarter et al. "Effect of large shear deformations on the fracture behavior of a fully pearlitic steel". *Metallurgical and Materials Transactions A: Physical Metallurgy and Materials Science*. Vol. 42. 6. Springer, June 2011, pp. 1609–1618.

[21] X. Zhang et al. Microstructure and strengthening mechanisms in cold-drawn pearlitic steel wire. *Acta Materialia* **59**.9 (May 2011), 3422–3430.

[22] Y. Ivanisenko et al. The mechanism of formation of nanostructure and dissolution of cementite in a pearlitic steel during high pressure torsion. *Acta Materialia* **51**.18 (Oct. 2003), 5555–5570.

[23] X. Zhang et al. Hierarchical structures in cold-drawn pearlitic steel wire. *Acta Materialia* **61**.13 (Aug. 2013), 4898–4909.

[24] J. E. Garnham and C. L. Davis. The role of deformed rail microstructure on rolling contact fatigue initiation. *Wear* **265**.9-10 (Oct. 2008), 1363–1372.

[25] L. Zhou et al. Comparison of the damage and microstructure evolution of eutectoid and hypereutectoid rail steels under a rolling-sliding contact. *Wear* **492-493** (Mar. 2022), 204233.

[26] H. Chen et al. Microstructure evolution of a hypereutectoid pearlite steel under rolling-sliding contact loading. *Materials Science and Engineering A* **655** (Feb. 2016), 50–59.

[27] T. Leitner et al. Influence of severe plastic deformation and specimen orientation on the fatigue crack propagation behavior of a pearlitic steel. *Materials Science and Engineering A* **710** (Jan. 2018), 260–270.

[28] T. Leitner, A. Hohenwarter, and R. Pippan. Anisotropy in fracture and fatigue resistance of pearlitic steels and its effect on the crack path. *International Journal of Fatigue* **124** (July 2019), 528–536.

[29] J. M. Hyzak and I. M. Bernstein. The role of microstructure on the strength and toughness of fully pearlitic steels. *Metallurgical Transactions A* **7**.8 (1976), 1217–1224.

[30] M. Dollar, I. M. Bernstein, and A. W. Thompson. Influence of deformation substructure on flow and fracture of fully pearlitic steel. *Acta Metallurgica* **36**.2 (Feb. 1988), 311–320.

[31] D. Nikas, X. Zhang, and J. Ahlström. Evaluation of local strength via microstructural quantification in a pearlitic rail steel deformed by simultaneous compression and torsion. *Materials Science and Engineering A* **737** (Nov. 2018), 341–347.

[32] T. Shinozaki et al. Influence of Lamellar Spacing on Deformation Behavior of Pearlite Steels Studied by In Situ Neutron Diffraction (July 2022).

[33] A. Kanie et al. Elastic Strains of Cementite in a Pearlite Steel during Tensile Deformation Measured by Neutron Diffraction. *ISIJ International* **44**.11 (Nov. 2004), 1952–1956.

[34] E. Gadalińska et al. Stress localisation in lamellar cementite and ferrite during elastoplastic deformation of pearlitic steel studied using diffraction and modelling. *International Journal of Plasticity* **127** (Apr. 2020), 102651.

[35] H. Yahyaoui et al. Effect of interlamellar spacing on the elastoplastic behavior of C70 pearlitic steel: Experimental results and self-consistent modeling. *Materials and Design* **55** (Mar. 2014), 888–897.

[36] Y. Wang et al. In-situ neutron diffraction during tension-compression cyclic deformation of a pearlite steel. *Materials Science and Engineering A* **676** (Oct. 2016), 522–530.

[37] Y. Tomota et al. Effect of carbon concentration on tensile behaviour of pearlitic steels. *Materials Science and Technology* **19**.12 (Dec. 2003), 1715–1720.

[38] F. Wetscher, R. Stock, and R. Pippan. Changes in the mechanical properties of a pearlitic steel due to large shear deformation. *Materials Science and Engineering A* **445-446** (Feb. 2007), 237–243.

[39] K. A. Meyer, M. Ekh, and J. Ahlström. Modeling of kinematic hardening at large biaxial deformations in pearlitic rail steel. *International Journal of Solids and Structures* **130-131** (2018), 122–132.

[40] D. Hull and D. J. Bacon. *Introduction to Dislocations*. Elsevier Ltd, 2011.

[41] M. A. Sutton, J.-J. Orteu, and H. W. Schreier. *Image Correlation for Shape, Motion and Deformation Measurements: Basic Concepts, Theory and Applications*. Boston, MA: Springer, 2010.

[42] S. Dhar et al. Multi-axial Fatigue of Head-Hardened Pearlitic and Austenitic Manganese Railway Steels: A Comparative Study. *Metallurgical and Materials Transactions A* **51**.11 (Nov. 2020), 5639–5652.

[43] J. A. Knut Andreas Meyer Daniel Gren and A. Ekberg. A method for in-field railhead crack detection using digital image correlation. *International Journal of Rail Transportation* **10**.6 (2022), 675–694. eprint: `https://doi.org/10.1080/23248378.2021.2021455`.

[44] EN13674-4. *Railway applications – Track – Rail – Part 4: Vignole railway rails from 27 kg/m to, but excluding 46 kg / m. EUROPEAN COMMITTEE FOR STANDARDIZATION*. Brussels, 2011.